Brodogradnja Volume 77 Number 4 (2026) 77414

University of Zagreb Faculty of Mechanical Engineering and Naval Architecture

journal homepage: www.brodogradnja.fsb.hr

Brodogradnja

An International Journal of Naval Architecture and Ocean Engineering for Research and Development

Parametric roll instability and roll reduction methods in oblique head seas

*Liu Liang[1] *, Luo Ruifeng[1,2,3], Chao Shifang[1,2], Yu Fuqiang[1,2], Zhang Baoji[4], Zhang Hao[4], Gong Jiaye[4], Liu Jie[5]*

[1]*Marine Engineering Research Institute, Shanghai Zhenhua Heavy Industries Co., Ltd., Shanghai, 200125, China*
[2]*National Engineering Research Center for Offshore Heavy Lift and Pipelay Core Equipment, Shanghai, 201913, China*
[3]*School of Ocean and Civil Engineering, Shanghai Jiao Tong University, Shanghai, 200240, China*
[4]*College of Ocean Science and Engineering, Shanghai Maritime University, Shanghai, 201306, China*
[5]*Ulsan Ship and Ocean College, Ludong University, Yantai, 264025, China*

ARTICLE INFO

Keywords:
Parametric roll
Self-propelled
Coupling effects
Oblique-wave
Roll-reduction

ABSTRACT

Numerical studies on parametric roll have mainly focused on head and following seas, whereas parametric roll in oblique head seas remains less fully understood due to the coupled effects of roll, sway, yaw, and the propulsion-steering system. In this study, a CFD-based numerical framework is developed for predicting parametric roll of a self-propelled KCS ship in oblique head seas, considering the coupled interactions among the hull, rudder, and propeller. The effects of model speed and wave heading on parametric-roll responses are investigated, and two mitigation strategies are examined, namely passive roll reduction using a bilge keel and active avoidance through speed control. The results show that parametric roll in oblique head seas is highly sensitive to model speed and wave heading. The roll response becomes pronounced when the encounter condition falls within the parametric-roll-sensitive range, whereas it is significantly weakened when the ship moves away from this range. Wave headings closer to head seas correspond to a more critical parametric-roll region. The bilge keel suppresses roll growth by increasing roll damping and reducing the roll moment, while speed control mitigates the nonlinear response by adjusting the encounter frequency. The present study demonstrates that CFD can be used not only to identify parametric-roll occurrence, but also to support the development of passive mitigation and active operational guidance for self-propelled ships in oblique head seas.

1. Introduction

Parametric roll is a roll motion induced by the periodic variation of a ship's underwater geometry, which in turn causes a periodic variation in the restoring moment and thereby excites roll oscillations [1]. Slender ships (e.g., container ships and truck carriers) are particularly susceptible to this phenomenon. In 2020, the International Maritime Organization (IMO) issued the Interim Guidelines on the Second Generation Intact Stability Criteria [2], in which parametric roll is identified as one of the five stability failure modes. This framework comprises three levels. Levels 1 and 2 employ simplified approaches to estimate, respectively, the

* Corresponding author.
E-mail address: liuliang3@zpmc.com

https://doi.org/10.21278/brod77414
Received 05 March 2026; Received in revised form 10 June 2026; Accepted 14 July 2026
Available online 04 September 2026
ISSN 0007-215X; eISSN 1845-5859

likelihood of occurrence and the response amplitude of parametric roll in head and following seas; in particular, averaging methods are applied to an uncoupled roll model with time-varying restoring terms. Level 3, by contrast, requires direct time-domain numerical simulations for parametric roll assessment. It should be noted that, to evaluate operational safety across different headings, Level 3 is required not only for head and following seas but also for oblique-wave conditions.

As early as the 1960s, parametric roll attracted sustained attention from the ship hydrodynamics community. Kerwin [3] employed a single-degree-of-freedom (DOF) roll model, representing the time variation of the righting arm (GZ) in regular longitudinal waves using trigonometric functions, and investigated the instability regions of parametric roll through a dynamic equation including both linear and nonlinear damping terms. Bulian [4] proposed an approximate frequency-domain analytical approach for a 1-DOF nonlinear roll model; by recasting the steady-state solution into a polynomial root-finding problem, the method successfully reproduced key nonlinear features in regular longitudinal waves, including the corresponding backbone curve. Based on a 1-DOF roll framework with nonlinear variations of the righting arm, Song et al. [5] analyzed parametric roll in both regular and irregular seas by introducing time-varying metacentric height and a nonlinear approximated GZ curve, thereby improving the assessment of instability boundaries and risk-related responses. Umeda et al. [6, 7] incorporated nonlinear characteristics of the wave-induced righting arm into a 1-DOF model to examine, respectively, the nonlinear response of GZ variations under head and following waves, and conducted a systematic comparison between the restoring moment computed under the Froude-Krylov assumption and constrained model-test measurements. Their results indicated that this theoretical approach exhibits pronounced discrepancies in predicting the amplitude of wave-induced GZ variations-particularly in head seas-thus failing to accurately capture the actual impact of waves on the ship's restoring capability. Using 1-DOF models, Schrøter and co-workers investigated several representative ship types and validated the applicability and effectiveness of the draft IMO Level 2 vulnerability criteria for parametric roll [8-12]. Somayajula et al. and Falzarano et al. [13, 14] developed procedures to quantify the occurrence probability of parametric roll in irregular seas by applying, respectively, Melnikov analysis and a stochastic approach based on first-passage-time statistics to the 1-DOF roll equation. The case studies showed that both methods yield consistent trends in risk assessment with respect to variations in significant wave height and peak period, capturing the influence of sea-state severity and characteristic frequency on instability probability reasonably.

Early prediction models for parametric roll predominantly relied on single-DOF roll equations, which became the mainstream due to their simple formulation and high computational efficiency. However, such models have limited capability to represent multi-DOF coupling effects-particularly the coupled influence of pitch and heave motions on roll response under wave excitation-thereby imposing intrinsic constraints on predictive accuracy. Since parametric roll is often accompanied by pronounced longitudinal motions, recent research has progressively shifted toward coupled multi-DOF prediction models to better capture nonlinear coupled ship motions in waves and the associated instability mechanisms. Silva et al. [15] developed a nonlinear time-domain coupled model that accounts for the contributions of pitch and heave to the time-varying restoring term in roll, and performed simulations in both regular and irregular head seas, demonstrating the pronounced influence of coupling on instability boundaries and amplitude growth. In longitudinal seas, Bulian [16] proposed a time-domain prediction approach in which the wave-induced righting-arm curve is analytically approximated and embedded into a 1.5-DOF roll framework: roll is solved dynamically as a single DOF, while pitch and heave are incorporated quasi-statically through hydrostatic corrections to the time-varying GZ. Neves et al. [17, 18] established a third-order nonlinear time-domain model coupling roll, pitch, and heave, and applied it to predict parametric roll of a fishing vessel with validation against experiments; the results highlighted that the prediction accuracy of the longitudinal DOFs (heave and pitch) is critical for reliable identification of parametric-roll instability. Rodríguez et al. [19, 20] conducted time-domain simulations of parametric roll for a large container ship using a nonlinear 3-DOF model (roll–heave–pitch) in regular and irregular head seas over different speeds and wave heights, and compared the results with 1:45 scale model tests. Their model reproduced the occurrence/non-occurrence of parametric roll reasonably well, although discrepancies remained in the pitch response for some conditions. Irkal et al. [21-23] systematically investigated the roll damping characteristics of ship hulls with and without bilge keels by combining free-roll decay experiments, PIV flow-field measurements, and URANS simulations. Their studies demonstrated that the URANS approach can be effectively used for roll damping prediction and for assessing the roll-reduction performance of bilge keels. Zhou et al. [24, 25] proposed a hybrid prediction strategy: roll damping was first obtained from CFD-based free-roll decay tests in calm water, and then combined with potential-flow hydrodynamic coefficients in a weakly nonlinear 3-DOF time-domain model to predict parametric roll in regular waves. Using a C11 container ship as the test case, Ma et al. [26] performed numerical simulations and experimental comparisons for parametric roll in head seas using both a three-dimensional time-domain potential-flow model and a RANS approach based on the STAR-CCM+ solver. When wave steepness was no greater than 0.03, both methods reproduced the instability region with good accuracy. As wave steepness increased, the potential-flow method exhibited markedly larger errors in amplitude prediction and critical-region identification, whereas the RANS results maintained better agreement with experiments, suggesting that the RANS-based CFD approach can more explicitly account for nonlinear flow effects and viscous contributions in large-amplitude roll responses. Li et al. [27, 28] and Liu et al. [29] also investigated parametric roll of different ship types using CFD, further corroborating the capability of CFD techniques in capturing large-amplitude nonlinear roll responses.

Existing numerical studies on parametric roll have mainly focused on head and following seas, where most models are formulated either as a single-DOF roll system or as a 3-DOF coupled system involving roll–pitch–heave. However, under oblique-wave conditions, the wave excitation contains not only pronounced longitudinal components but also significant lateral components. In this context, a 3-DOF model alone is often insufficient to represent the dynamic characteristics of parametric roll in oblique waves. Umeda et al. [30] incorporated low-speed manoeuvring hydrodynamic forces based on coupled roll-heave-pitch motions and developed a 5-DOF model. Comparison with free-running model tests showed that the 5-DOF model could reproduce the unstable region and the trend of amplitude growth, but it tended to overpredict the maximum roll amplitude in bow-quartering waves by approximately 7°, corresponding to a maximum relative error of about 35% with respect to the maximum roll amplitude measured in the model tests. Sakai et al. [31] proposed an averaging-based procedure to estimate parametric-roll amplitudes in both longitudinal and oblique waves: the approach applies an averaging technique to an uncoupled roll equation and improves the representation of restoring characteristics by fitting the calm-water GZ curve; it also provides an estimate of the critical speed and further extends the method to oblique waves by accounting for the effects of ship speed and heading, with validation against numerical calculations and free-running model experiments. Gu et al. [32] investigated a C11 container ship and developed a time-domain prediction model based on a three-dimensional hybrid panel method, conducting numerical simulations of the motion responses in bow-quartering waves for both 3-DOF and 6-DOF configurations. Their results indicated that the 3-DOF mathematical model yields somewhat conservative predictions for the parametric-roll vulnerability mode. Overall, numerical investigations of parametric roll in oblique waves remain relatively limited, partly because the coupling between seakeeping and manoeuvring effects is unavoidable in such conditions.

To address the aforementioned limitations, this study develops a six-degree-of-freedom (6-DOF) motion model that accounts for the coupled interactions among the hull, rudder, and propeller, and performs CFD simulations of parametric roll for the self-propelled KCS container ship in oblique head seas. First, self-propulsion computations in calm water are carried out to determine the propeller rotational speed corresponding to the self-propelled condition adopted in the parametric-roll simulations. Second, under oblique head-wave conditions, the parametric-roll responses at different ship speeds are analyzed to examine the influence of speed variation on the nonlinear instability development. Subsequently, the effects of wave heading are systematically investigated by comparing the amplitude-growth behavior and the resulting steady-state characteristics of parametric roll. Finally, from the perspectives of passive mitigation and active avoidance, the effects of a bilge keel and speed control on parametric roll are evaluated, and their underlying roll-reduction mechanisms are discussed.

2. Modeling and computational setup

2.1 Geometry and simulation conditions

The KCS container ship is selected as the test case in this study. To facilitate overset-grid generation, the connection regions between the hull and the rudder/propeller are appropriately simplified while preserving the key flow features and the associated hydrodynamic interaction effects. Specifically, some small-scale geometric details are removed, which improves mesh quality and reduces discontinuities in the overset-interpolation region, thereby enhancing interpolation accuracy and numerical robustness. Figure 1 illustrates the geometric model of the KCS ship equipped with a propeller and rudder, and the principal particulars are listed in Table 1. As shown in the figure, the x-axis is aligned with the ship length and points toward the bow, the y-axis points to port, and the z-axis is positive upward.

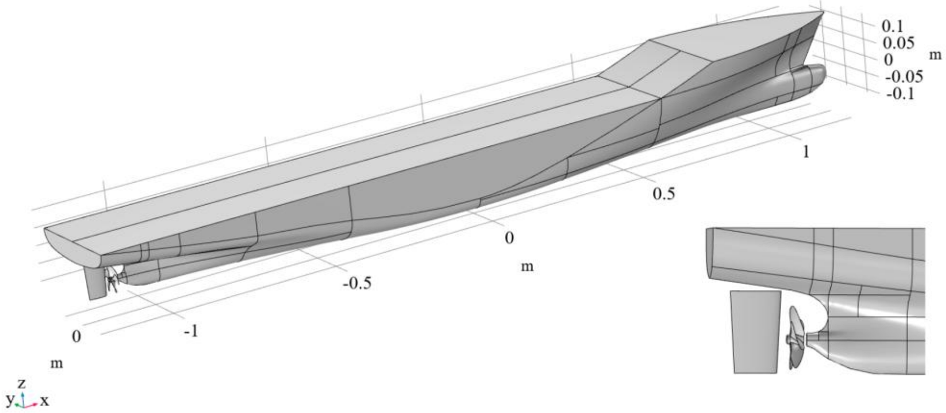

Fig. 1 Three-dimensional geometric model of the self-propelled KCS ship

Referring to the model-test conditions, numerical simulations of parametric roll were carried out for the KCS model under head-sea and oblique head-sea conditions. The detailed computational cases are listed in Table 2. Here, Fn denotes the Froude number, which is defined as follows:

$$Fn = \frac{V_m}{\sqrt{gL_{PP}}} \tag{1}$$

where V_m is the model speed, g is the gravitational acceleration, and L_{PP} is the model-scale length between perpendiculars.

The encounter frequency is calculated as:

$$f_e = f_w - \frac{V_m}{\lambda}\cos\beta \tag{2}$$

where f_e is the encounter frequency, f_w is the wave frequency, λ is the wavelength, and β is the wave heading angle.

Table 1 Geometrical particulars of KCS

Project	Main dimension	Full scale	Model scale
	Scale	1:1	1:100
	Length between perpendiculars, L_{PP} (m)	230	2.300
	Breadth, B (m)	32.2	0.322
	Depth, D_H (m)	19.0	0.190
	Draft, d (m)	10.8	0.108
	Volume (m^3)	52030	0.0520
	Mass (Kg)	5.203×10^7	52.030
Hull	Longitudinal position of Center of Buoyancy, LCB(m)	111.6	1.116
	Metacentric height, GM(m)	1.290	0.0129
	Radius of gyration, roll, K_{XX}/B	0.346	0.3246
	Radius of gyration, pitch, yaw, K_{YY}/L_{PP}, K_{ZZ}/L_{PP}	0.248	0.249
	Natural roll period, (s)	21	2.10
	Natural pitch period, (s)	7.7	0.77
	Rudder height, (m)	9.9	0.099
Rudder	Area, (m^2)	54.45	0.054
	Aspect ratio	1.8	1.8
	Number of blades	5	5
Propeller	Diameter, D_P (m)	7.9	0.079
	Direction of rotation	Right-handed	Right-handed
	Aft-end distance to midship, (m)	36.5	0.365
Bilge keel	Forward-end distance to midship, (m)	33.0	0.33
	Breadth, B_{bk} (m)	1.0	0.01

Table 2 Summary of simulation conditions

V_m (m/s)	F_n	β (deg)	λ (m)	f_w (Hz)	f_e (Hz)	Parametric rolling
0.5	0.105	150	2.3	0.824	1.012	Yes
0.6	0.126	150	2.3	0.824	1.050	Yes
0.7	0.147	150	2.3	0.824	1.087	Yes
0.8	0.168	150	2.3	0.824	1.125	Yes
0.85	0.179	150	2.3	0.824	1.144	No
0.7	0.147	165	2.3	0.824	1.118	Yes
0.8	0.168	165	2.3	0.824	1.160	Yes
0.85	0.179	165	2.3	0.824	1.181	Yes
0.9	0.189	165	2.3	0.824	1.202	No
0.7	0.147	180	2.3	0.824	1.128	Yes
0.8	0.168	180	2.3	0.824	1.172	Yes
0.9	0.189	180	2.3	0.824	1.215	Yes
0.95	0.200	180	2.3	0.824	1.237	Yes
1.0	0.211	180	2.3	0.824	1.259	No

2.2 Governing equations

In this study, CFD simulations are performed using the open-source code OpenFOAM. Within the URANS framework, the governing equations are solved in the liquid phase and can be written as follows:

$$\frac{\partial \overline{u}_j}{\partial x_j} = 0 \tag{3}$$

$$\frac{\partial \overline{u}_i}{\partial t} + \overline{u}_j \frac{\partial \overline{u}_i}{\partial x_j} = -\frac{1}{\rho}\frac{\partial \overline{p}}{\partial x_i} + \nu \frac{\partial^2 \overline{u}_i}{\partial x_j^2} - \frac{\partial \overline{u_i' u_j'}}{\partial x_j} + f_i \tag{4}$$

In the above equations, u_i denotes the velocity components in the x, y, z directions ($i, j = 1,2,3$, with the Einstein summation convention applied to repeated indices); p is the pressure; $\nu = \mu / \rho$ is the kinematic viscosity; and f_i represents the source term per unit volume (i.e., body force). The term $\overline{u_i' u_j'}$ is the Reynolds-stress tensor, accounting for the additional momentum transport induced by turbulent fluctuations. In this study, the governing equations are closed using the shear stress transport $SST\,k-\omega$ turbulence model. Previous studies have shown that, compared with the $k-\varepsilon$ model, the $SST\,k-\omega$ model provides more accurate predictions of the wake field and boundary-layer development [33]. In addition, the model has been validated by Sadat-Hosseini et al. [34], demonstrating satisfactory performance in predicting model-scale parametric roll. Therefore, the $SST\,k-\omega$ model is adopted herein for the numerical simulation of parametric roll motion.

Two coordinate systems are employed in this study: an earth-fixed (inertial) coordinate system and a ship-fixed coordinate system, as illustrated in Figure 2. The ship motions are described in the earth-fixed coordinate system, while the ship-fixed coordinate system is attached to the ship's center of gravity and moves together with the vessel.

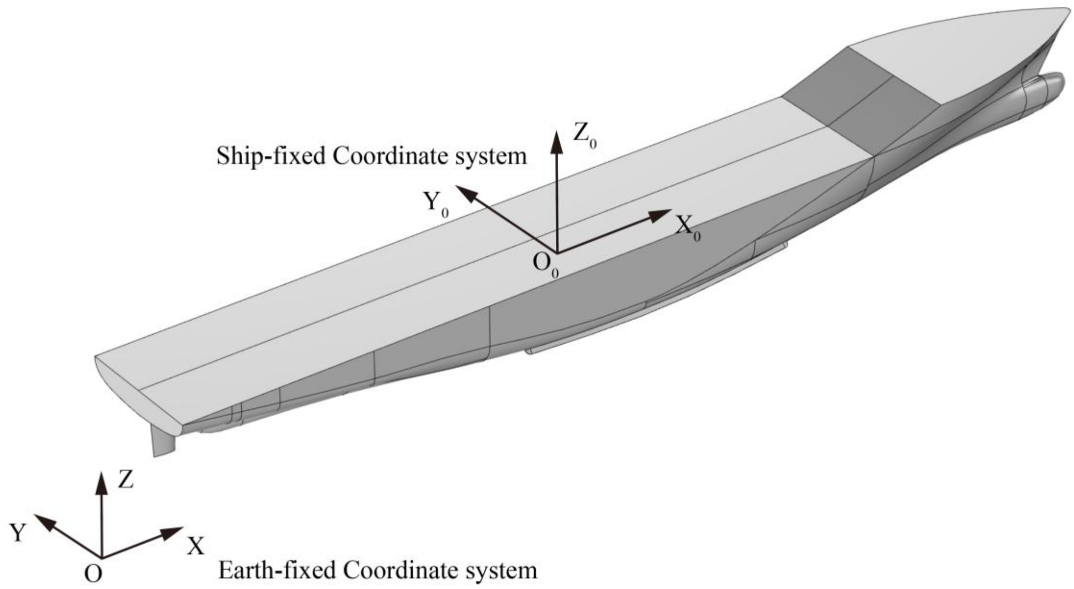

Fig. 2 Coordinate Systems

2.3 Overset-grid computational model

When performing numerical simulations of parametric-roll instability in oblique head seas, the asymmetric excitation induced by obliquely incident waves causes the ship to exhibit not only the characteristic roll response but also pronounced sway and yaw motions. In addition, compared with head seas, wave propagation in oblique conditions contains a stronger transverse component; therefore, to mitigate wave reflection and energy loss during propagation, a rectangular numerical wave tank is adopted to solve the flow field around the ship under parametric-roll conditions. The computational domain and boundary conditions are illustrated in Figure 3. In the ship-fixed coordinate system, the domain extents are $-2.5L_{PP} < X < 1.5 L_{PP}$, $-2.0 L_{PP} < Y < 2.0 L_{PP}$, $-1.5 L_{PP} < Z < 1.0 L_{PP}$. Regarding boundary conditions, a velocity-inlet boundary with zero pressure gradient is used to represent the far-field inflow, while a pressure-outlet condition is imposed at the downstream boundary. Since the flow is simulated under self-propulsion, the ship advances forward, driven by the propeller; hence, the ship's forward speed is not superimposed on the inlet velocity. To suppress wave reflection and prevent contamination of the near-field flow around the ship, wave-damping zones are applied on all boundaries except the top and bottom surfaces of the computational domain. No-slip wall boundary conditions are imposed on the hull and appendage surfaces. The free surface is captured using the VOF method throughout the simulations.

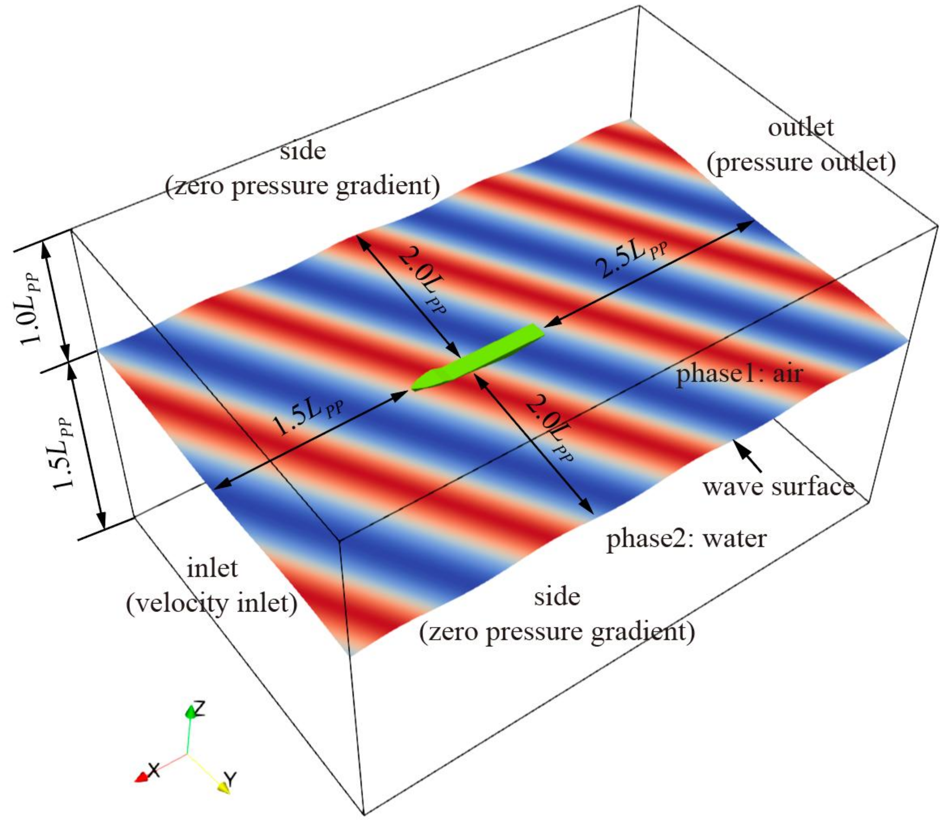

Fig. 3 Numerical wave tank for simulations in oblique head seas

For the numerical wave tank, the background mesh is generated using blockMesh and discretized with a structured hexahedral grid. To improve the resolution of wave propagation and free-surface deformation near the interface, local refinement is applied in the vicinity of the free surface. Specifically, each wavelength is resolved by 60 cells along the wave-propagation direction, and 30 grid nodes are used in the wave-height direction, ensuring adequate numerical accuracy for wave evolution under different wave-heading conditions. Given the complex geometry in the vicinity of the hull and appendages (e.g., rudder), snappyHexMesh is employed to generate an unstructured body-fitted mesh on the surfaces, and boundary-layer cells are created near solid walls to satisfy the resolution requirements of the viscous sublayer. In particular, to ensure that the first-layer cell thickness meets the wall-resolution criterion of ($y+ \leqslant 1$), the first-layer height Δs is determined according to Equation (5). Based on the computed Δs, a multilayer boundary-layer mesh is generated with an expansion ratio of 1.2, providing sufficient grid resolution for accurately capturing viscous forces and velocity gradients. After independently meshing the main hull, appendages, and background domain, an overset region with a prescribed thickness is constructed in space, and the mesh components are combined to form the overset-grid computational model for simulating the unstable parametric roll motion under oblique-wave conditions, as shown in Figure 4.

$$\Delta s = \frac{y^+ L_{PP}}{Re\sqrt{\frac{C_f}{2}}} \tag{5}$$

where C_f is the friction coefficient, which can be evaluated using the ITTC formula, and Re is the Reynolds number.

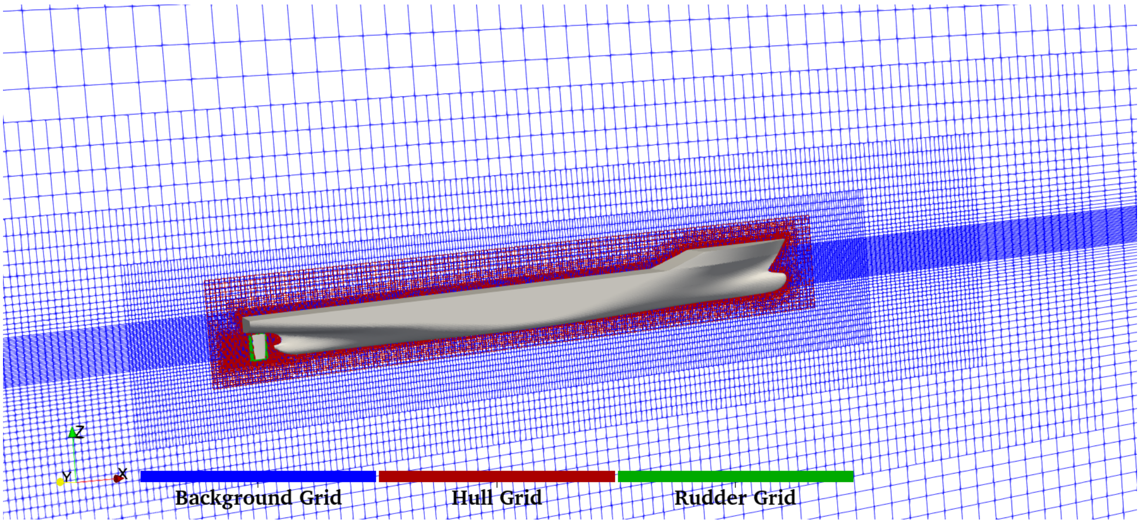

Fig. 4 Overset grid of numerical model

2.4 Hull-rudder-propeller coupling

To enable numerical simulations of the coordinated motions of the hull, rudder, and propeller, a hierarchical multi-body motion framework is developed to consistently describe the relative kinematic relationships among all moving components, as shown in Figure 5. The framework is organized into three motion levels. The first-level motion corresponds to the translation of the numerical wave tank in the surge and sway directions, together with a yaw rotation. This level is introduced to keep the relative position between the wave-tank mesh (i.e., the background mesh) and the hull mesh approximately invariant, thereby maintaining the interpolation quality within the overset region. The second-level motion represents the six-degree-of-freedom (6-DOF) motion of the hull relative to the numerical wave tank (i.e., in the inertial frame), including surge, sway, heave, roll, pitch, and yaw. This level describes the rigid-body motion of the hull-fixed coordinate system with respect to the inertial coordinate system. The third-level motion refers to the local motions of hull appendages (e.g., the propeller and rudder) relative to the hull in the hull-fixed frame. Specifically, the propeller performs a prescribed periodic rotation about its shaft axis, while the rudder rotates about the rudder stock to achieve the commanded rudder angle for maneuvering. It should be noted that, while executing the third-level rotational motions, the propeller and rudder simultaneously participate in the second-level 6-DOF motion of the hull, resulting in a compound translational-rotational motion in the inertial coordinate system.

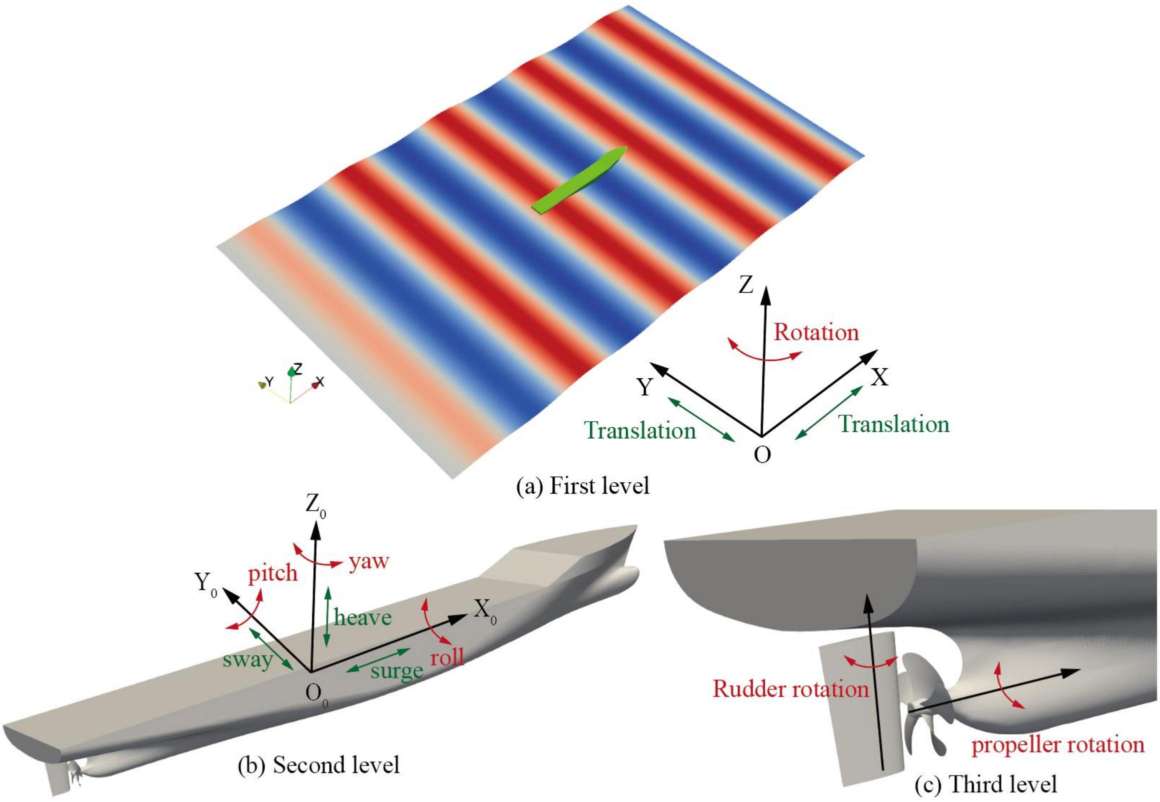

Fig. 5 Schematic of the coupled hull-rudder-propeller motion framework

To ensure adequate course-keeping capability of the ship under wave conditions, a maneuvering control module for heading keeping is developed in this study. During the control process, a proportional-integral-derivative (PID) controller [35, 36] is employed, which can be written as:

$$\delta(t) = Pe_{\varphi}(t) + I\int_0^t e_{\varphi}(t)dt + D\frac{de_{\varphi}(t)}{dt} \tag{6}$$

$$e_{\varphi}(t) = \varphi_c - \varphi(t) \tag{7}$$

where P, I, and D are the proportional, integral, and derivative gains, respectively, $e_{\varphi}(t)$ denotes the error between the predicted heading angle $\varphi(t)$ and the target heading φ_c, and $\delta(t)$ is the rudder angle.

Similarly, the propeller rotational speed is adjusted using a PID controller to ensure that the ship reaches the prescribed forward speed during free-running simulations and to obtain the corresponding propeller rate. Accordingly, Equations (6) and (7) are rewritten as:

$$n(t) = Pe_U(t) + I\int_0^t e_U(t)dt + D\frac{de_U(t)}{dt} \tag{8}$$

$$e_U(t) = U_{\text{target}} - U(t) \tag{9}$$

where $e_U(t)$ is the error between the predicted ship speed $U(t)$ and the target speed U_{target}, and $n(t)$ denotes the instantaneous propeller rotational speed.

Modeling the propeller thrust is a key step for reproducing the stern-flow structure and for accurately predicting maneuvering responses. To represent the suction effect induced by the propeller in the stern region, a body-force propeller model is adopted in this study. In this approach, a virtual disk is introduced at the propeller plane to replace the real blades, and an equivalent axial volumetric force field is imposed within the disk region to account for the mean propulsive effect. The disk diameter is set equal to the actual propeller diameter, while its thickness is taken as an effective value corresponding to the lateral projected dimension of the blades; the disk axis is aligned with the rotation axis of the discretized propeller. Since this method does not require blade-resolved meshing, it enables higher computational efficiency. The actuator-disk modeling strategy is illustrated in Figure 6.

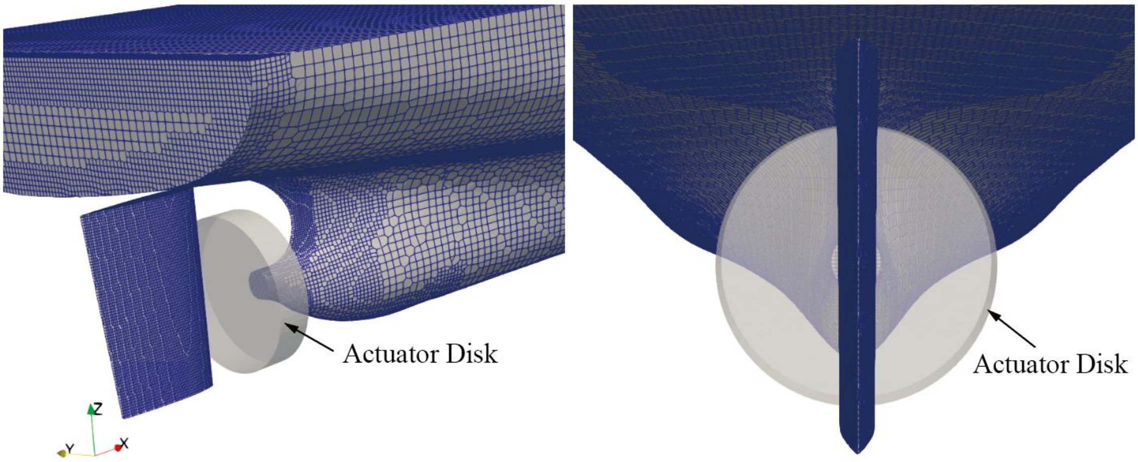

Fig. 6 Body-force (actuator-disk) propeller modeling approach

3. Self-propulsion simulations

To determine the propeller rotational speed corresponding to the self-propulsion condition during parametric roll in oblique head seas, a series of calm-water self-propulsion simulations is first performed to establish the thrust-speed matching relationship. As a prerequisite, the propeller open-water characteristics are computed to obtain the performance curves under different advance conditions. In this study, the KP505 propeller is simulated at the same model scale as that adopted in the KP505 open-water experiments from the SIMMAN 2020 international CFD workshop, and the numerical predictions are validated against the experimental measurements [37]. The KP505 open-water simulations are carried out in a rectangular computational domain, and the domain size as well as the boundary conditions are illustrated in Figure 7.

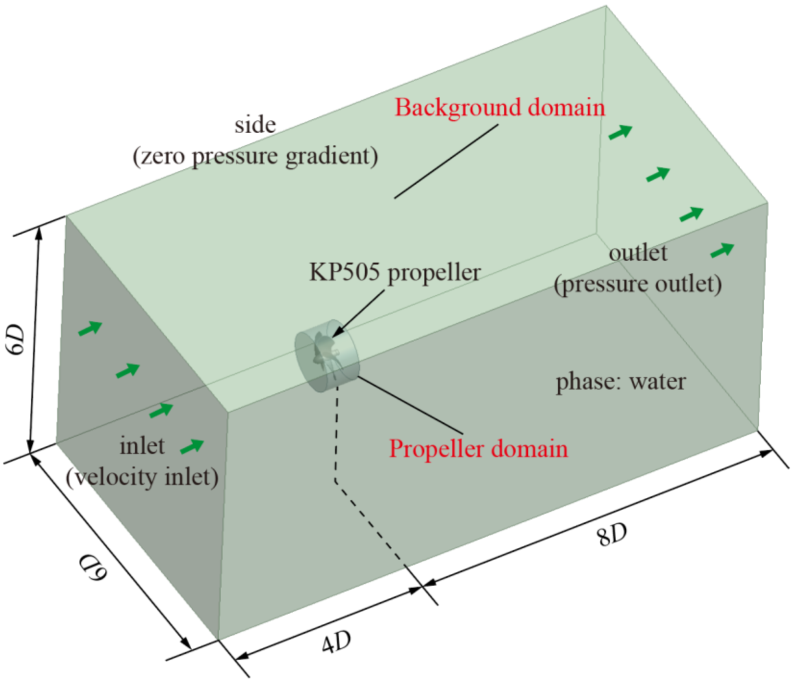

Fig. 7 Computational domain and boundary conditions for the KP505 open-water simulations

During the numerical simulations of the propeller open-water test, the propeller rotational speed is kept constant, and the advance coefficient J is varied by adjusting the inflow velocity V_A. The hydrodynamic performance of a propeller is commonly characterized by three nondimensional coefficients, namely the thrust coefficient K_T, the torque coefficient K_Q, and the open-water efficiency η_0, which are defined as:

$$J = \frac{V_A}{D_P n} \tag{10}$$

$$K_T = \frac{T}{\rho n^2 D_P^4} \tag{11}$$

$$K_Q = \frac{Q}{\rho n^2 D_P^5} \tag{12}$$

$$\eta_0 = \frac{J}{2\pi} \cdot \frac{K_T}{K_Q} \tag{13}$$

Here, T and Q denote the thrust and torque generated by the propeller, respectively; ρ is the fluid density, n is the propeller rotational speed, and D_P is the propeller diameter.

Figure 8 presents the CFD-predicted open water performance of the KP505 propeller under different advance coefficients. As the advance coefficient increases, both the thrust coefficient and the torque coefficient decrease monotonically, which is consistent with the typical hydrodynamic characteristics of marine propellers. Moreover, the numerical predictions show good agreement with the experimental data, with a maximum relative error of less than 3.7%.

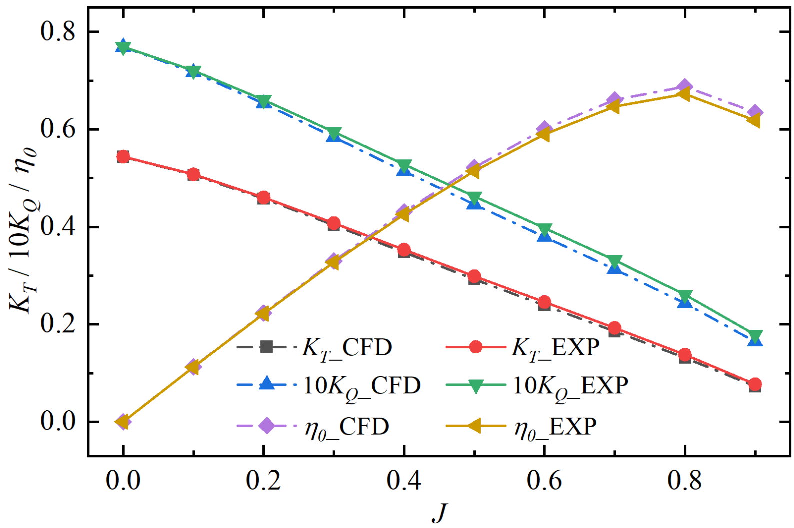

Fig. 8 Open water performance curves of the KP505 propeller

Then, the calm-water resistance performance of the KCS hull was predicted using CFD under the following conditions: model speed V_m = 2.196 m/s, Fr = 0.26, Re = 1.26×10^7. The numerical results of the calm-water resistance are summarized in Table 3 and compared with the towing-tank experimental data reported in the CFD workshop database [38, 39]. The comparison shows that the relative error of the total resistance coefficient C_T is less than 2 %, while the relative error of the pressure resistance coefficient C_P is less than 3 %, indicating good agreement between the numerical predictions and the experimental measurements. The frictional resistance coefficient C_F in the experiments is calculated using the ITTC-1957 correlation line [40] as follows:

$$C_F = \frac{0.075}{(\log_{10} R_e - 2)^2} \tag{14}$$

Table 3 Comparison of calm-water resistance results

Project	CFD	EXP	Error
C_T	3.658×10^{-3}	3.711×10^{-3}	-1.428 %
C_P	0.697×10^{-4}	7.180×10^{-4}	-2.924 %
C_F	2.961×10^{-3}	2.993×10^{-3}	-1.069 %

Figure 9 shows the free-surface wave pattern predicted by the CFD simulation. Overall, no discontinuities caused by overset interpolation are observed within the overset region of the free surface, indicating that the mesh quality is satisfactory and that the interpolation algorithm exhibits good stability and accuracy. To further quantify the agreement between the numerical predictions and the experimental data, Figure 10 presents the comparison of wave elevations at two longitudinal sections (y = 0.0741L_{PP} and y = 0.1509L_{PP}). From the near field to the far field, the numerically predicted free-surface profiles are in good agreement with the measured data, accurately capturing the variation of the wave pattern during propagation. This result further confirms the applicability and effectiveness of the overset-grid method in simulating free-surface wave propagation.

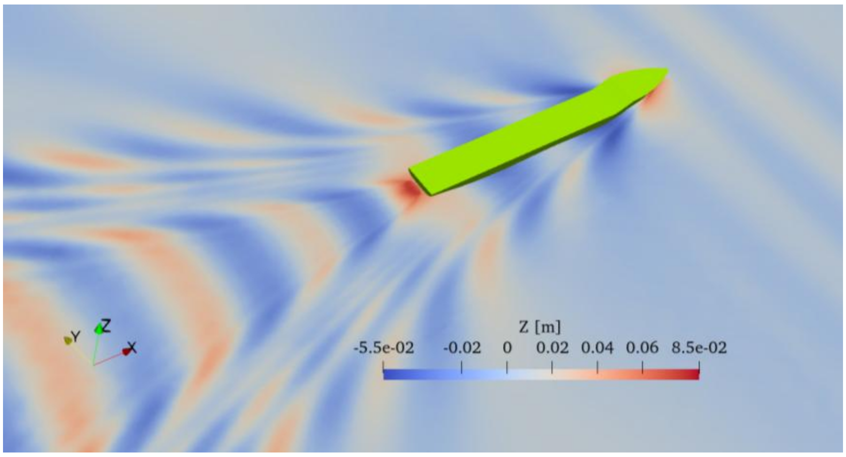

Fig. 9 Free-surface wave pattern of the KCS hull in calm water

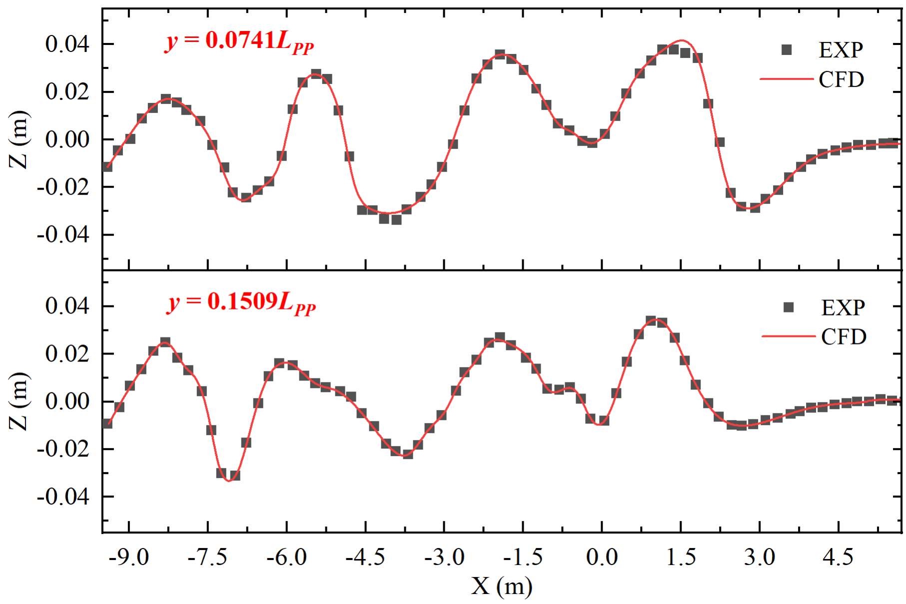

Fig. 10 Comparison of wave elevations at different free-surface sections

After validating the propeller open-water characteristics and the hull resistance performance, numerical simulations and response analyses of the self-propulsion performance of the KCS hull were carried out. In the self-propulsion simulations, the translational degree of freedom in the longitudinal (x) direction and the rotational degree of freedom about the transverse (y) axis were released, allowing the ship to respond naturally to the propeller thrust. During the simulations, the propeller rotational speed was adjusted in real time by the PID controller developed in Section 2.4 to regulate the model speed. The PID controller was activated at the start of the simulation and updated the propeller rotational speed at every time step according to the instantaneous speed error. Through this closed-loop control strategy, the ship continuously accelerated under the action of propeller thrust and eventually reached the target speed.

Figure 11 presents the time histories of the propeller rotational speed and model speed for the case of $Vm = 0.5$ m/s, with a total simulation time of 16s. As shown in the figure, the PID controller was able to adjust the propeller rotational speed in real time according to the deviation between the instantaneous model speed and the prescribed target speed, thereby effectively driving the model speed toward the desired value. In the initial stage, the ship underwent a distinct acceleration process; thereafter, the speed gradually converged and reached the target value at approximately t = 9s. The overall self-propulsion response exhibits satisfactory dynamic behavior and stable convergence.

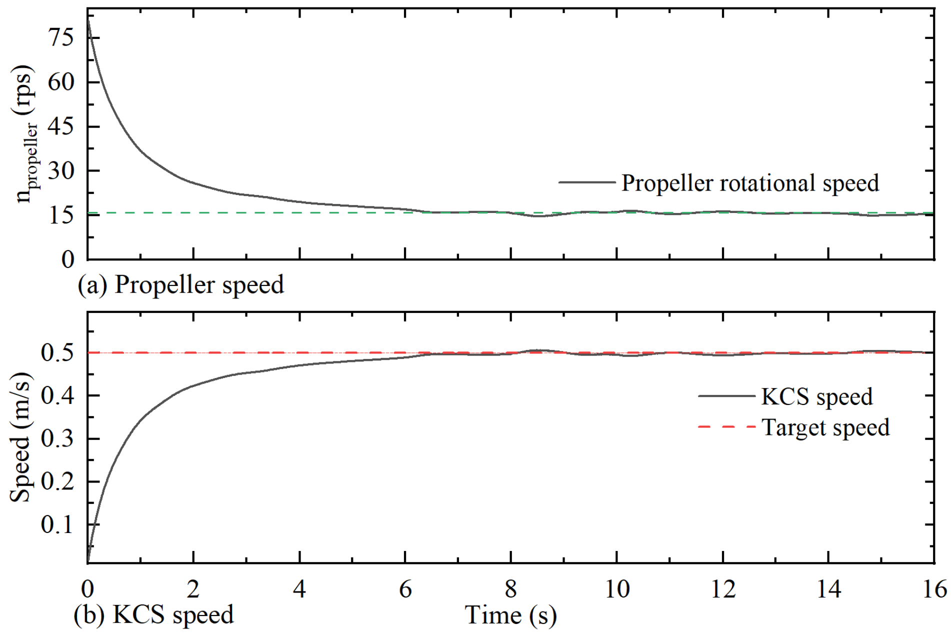

Fig. 11 Time histories of the propeller rotational speed and model speed during the self-propulsion simulation

Based on the previously established calm-water self-propulsion procedure, the self-propulsion conditions of the KCS model were determined over the target speed range (V_m = 0.4-0.8 m/s), and the corresponding steady-state propeller rotational speeds were obtained, as shown in Figure 12. To ensure physical consistency of the input boundary conditions in the subsequent CFD simulations in waves, the propeller rotational speed adopted in the parametric-roll simulations under oblique head seas was prescribed as the steady self-propulsion speed obtained in calm water through PID control. The primary purpose of this treatment is to eliminate the interference of waves on the propulsion system, so that the numerical simulations can more accurately represent the pure motion response of the hull in waves at a given forward speed. By determining the propeller rotational speed in advance, the propulsion system can be maintained in a stable operating state throughout the simulations, making the numerical setup more consistent with the experimental conditions. In addition, prescribing the calm-water self-propulsion rotational speed avoids additional disturbances induced by propeller-speed fluctuations during the simulation, thereby improving the stability and repeatability of the numerical results.

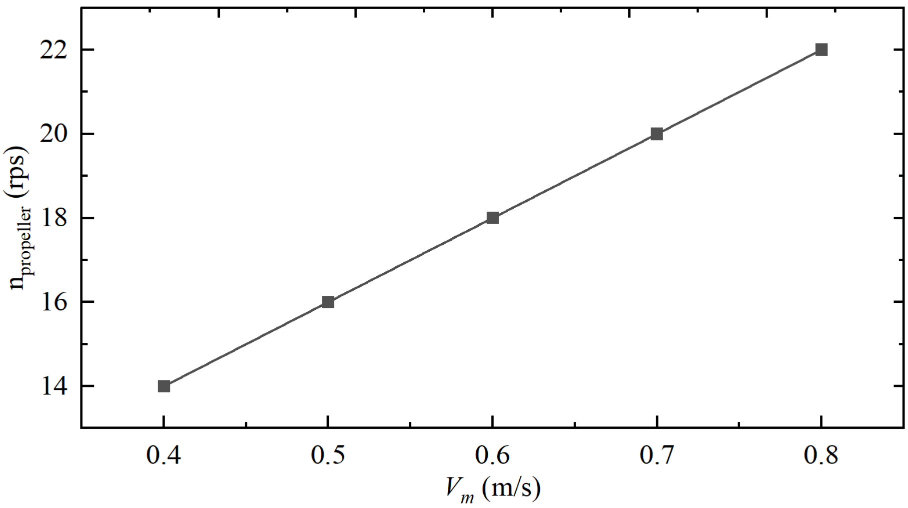

Fig. 12 Propeller rotational speeds corresponding to the self-propulsion points of the KCS model at different model speeds

4. Results and discussion

4.1 Numerical validation and sensitivity analysis

To evaluate the influence of spatial discretization error on the numerical prediction of parametric roll, three grid systems with different resolutions were generated using a grid-refinement ratio of $\sqrt{2}$. The grid-convergence analysis was conducted for the validation condition consistent with the model test, namely $\lambda/L_{PP} = 1.0$, $H_w/\lambda = 0.02$, and $V_m = 0.5$ m/s. Since parametric roll is a typical nonlinear instability phenomenon, its response generally involves an initial disturbance stage, an amplitude-growth stage, and a saturated large-amplitude stage. A single instantaneous peak may be affected by phase differences and initial disturbances. Therefore, the roll amplitude in the saturated stage was adopted as the evaluation quantity for the grid-independence assessment. Figure 13 shows the roll time histories obtained with different grid resolutions. It can be observed that all three grid systems capture the main response process of parametric roll, including the growth of roll amplitude from small disturbances and the subsequent development into a large-amplitude periodic response. This indicates that the present numerical model can reproduce the main motion characteristics of parametric-roll instability. As the grid is refined, the numerical results gradually approach the experimental result, suggesting that the influence of spatial discretization error on the predicted roll amplitude is reduced. Table 4 further presents a quantitative comparison of the roll amplitudes in the saturated stage under different grid resolutions. The roll amplitudes predicted by the coarse, medium, and fine grids are 26.34°, 25.70°, and 25.40°, respectively, while the experimental value is 24.82°. The corresponding errors are 6.12 %, 3.54 %, and 2.33 %, respectively. The difference between the medium-grid and fine-grid results is only 0.30°, indicating that further grid refinement has a limited influence on the predicted roll amplitude and that the numerical solution has essentially reached a grid-independent state. Considering both computational accuracy and cost, the medium grid was adopted for the subsequent simulations.

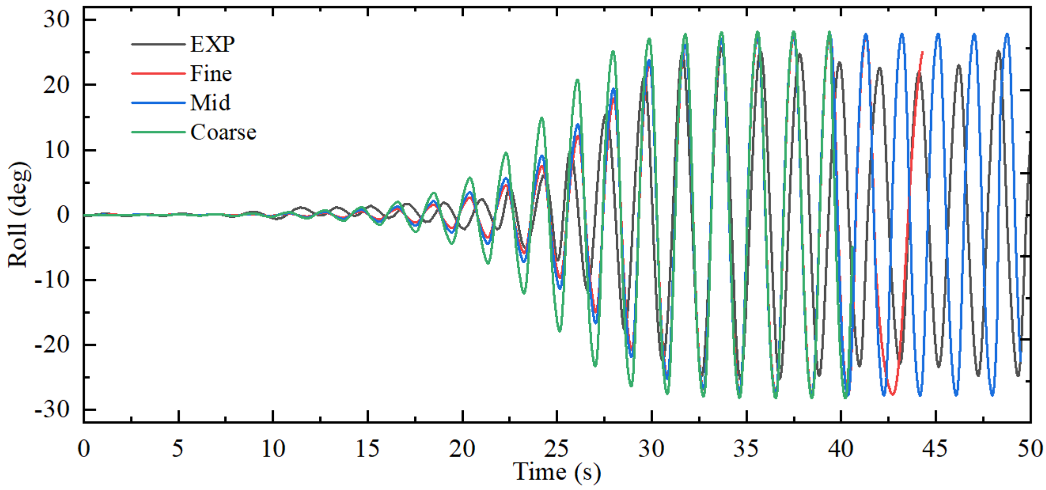

Fig. 13 Comparison of parametric-roll responses obtained with different grid resolutions

Table 4 Numerical comparison of parametric-roll responses under different grid resolutions

Grid	Cell (M)	Φ (deg)	Error (%)
Coarse	2.87	26.34	6.12
Medium	5.19	25.70	3.54
Fine	10.25	25.40	2.33
EFD	—	24.82	—

In addition to spatial discretization error, the choice of turbulence model may also affect the numerical prediction of parametric roll, particularly through its influence on the prediction of near-wall boundary-layer development during large-amplitude roll motion. To further assess the applicability of the turbulence model used in this study, a sensitivity analysis was conducted using three commonly adopted turbulence models, namely the standard k-epsilon, realizable k-epsilon, and SST k-omega models. The corresponding parametric-roll time histories and quantitative comparison are shown in Figure 14 and Table 5, respectively. As shown in Figure 14, all three turbulence models can reproduce the overall response process of parametric roll, including the gradual growth of roll amplitude and the subsequent saturated oscillation. However, noticeable differences are observed in the predicted roll amplitudes. According to Table 5, the maximum roll amplitude measured in the model test is 24.82°. The maximum roll amplitudes predicted by the standard k-epsilon, realizable k-epsilon, and SST k-omega models are 27.56°, 26.51°, and 25.70°, respectively, corresponding to errors of 11.03%, 6.80%, and 3.54%. Among these models, the SST k-omega model provides the closest agreement with the experimental result. From a physical perspective, the parametric-roll problem considered in this study involves large-amplitude roll motion, nonlinear free-surface variation, near-wall flow around the hull, and possible local flow separation near the bilge region and appendages. These factors are closely related to roll damping, viscous energy dissipation, and the roll-moment response. Compared with the k-epsilon-based models, the SST k-omega model is more suitable for predicting near-wall flow and separated flow under adverse pressure gradients and is therefore more appropriate for resolving the viscous-flow characteristics around the hull during large-amplitude roll motion. Accordingly, based on the grid-independence assessment, turbulence-model sensitivity analysis, and comparison with the model-test results, the medium grid and the SST k-omega turbulence model were adopted for the subsequent parametric-roll simulations.

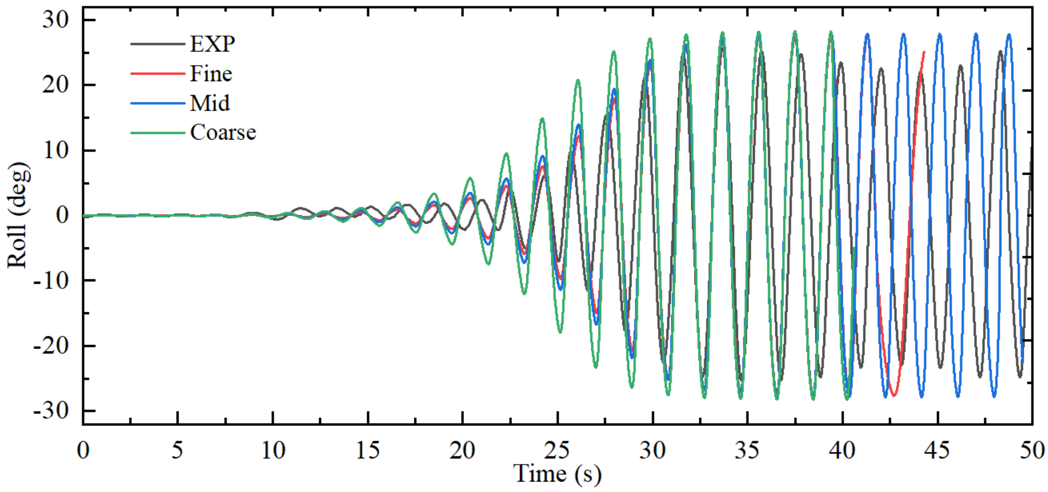

Fig. 14 Parametric-roll time histories obtained with different turbulence models

Table 5 Numerical results of parametric-roll simulations obtained with different turbulence models

Turbulence model	Roll (deg)	Experimental (deg)	Error (%)
Standard K- epsilon	27.56	24.82	11.03
Realizable K- epsilon	26.51	24.82	6.80
SST K- omega	25.70	24.82	3.54

4.2 Analysis of parametric roll instability at different model speeds

In oblique head seas, the wave direction forms an angle with the ship bow, so that the wave excitation contains not only a pronounced longitudinal component but also a stronger lateral component, making the roll-excitation conditions more complex. Under such circumstances, variations in model speed affect not only the encounter frequency but also the manner in which the ship encounters the incoming waves, thereby influencing the excitation characteristics and the establishment and persistence of resonance conditions. As a result, speed variation in oblique head seas may lead to roll-response characteristics that differ substantially from those in pure head seas. On this basis, it is necessary to further investigate the parametric-roll response of the ship at different forward speeds in oblique head seas, with particular emphasis on its influence on the growth of roll amplitude, response stability, and the onset of instability.

Figure 15 shows the free surface elevation and ship attitude at several representative instants for the case of an oblique head-wave incidence angle of 150°, a wavelength ratio of λ/L_{PP} = 1.0, and a model speed of V_m = 0.7 m/s. It can be observed that, during the initial stage (Figures 15(a)-15(c)), the free-surface pattern around the ship remains relatively regular, with uniformly distributed crests and troughs, and only a slight roll response is observed. This indicates that, under the initial wave excitation, the free surface has not yet developed noticeable asymmetry, and the accumulation of roll energy is still limited. As time progresses, the free-surface pattern gradually changes. In the intermediate and later stages shown in Figures 15(d)-15(i), the free surface on the two sides of the ship becomes markedly asymmetric: the wave crest on one side rises locally, while the corresponding trough on the other side deepens, accompanied by a clear increase in the roll angle. These observations indicate that, under the combined influence of wave excitation and changes in ship attitude, the roll motion experiences a pronounced amplification, and the ship enters the large-amplitude roll stage following the initial development of instability.

Figure 16 further presents the time history of the roll angle over the corresponding period, with the representative instants shown in Figure 15 marked on the curve. It can be observed that, during 0 ~ 25s, the roll amplitude does not decay within a short time; instead, it undergoes a development process from small-amplitude oscillations to rapid amplification. In the initial stage, the roll response remains relatively mild. In the intermediate and later stages, the roll amplitude increases markedly and gradually develops into a large-amplitude periodic oscillation. This process should not be interpreted simply as a transient response caused by the initial incident-wave disturbance. Rather, it results from the combined effects of wave-induced variations in the instantaneous underwater geometry of the hull, unsteady changes in the roll restoring moment, and direct roll excitation caused by oblique waves. Among these effects, the periodic variation of the roll restoring characteristics provides the main energy-input path for the sustained growth of the roll amplitude, while the direct roll excitation induced by oblique waves further affects the local response characteristics of the roll motion.

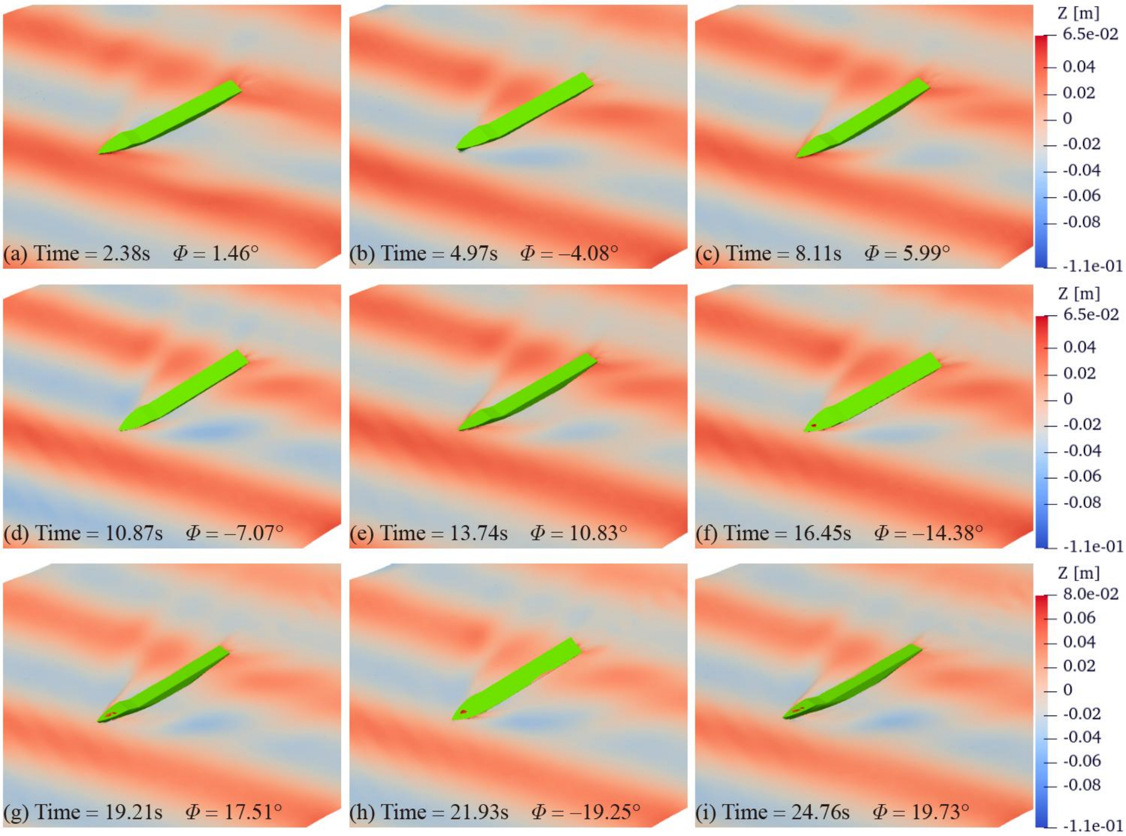

Fig. 15 Evolution of the free surface pattern during parametric roll instability under the 150° oblique head wave condition

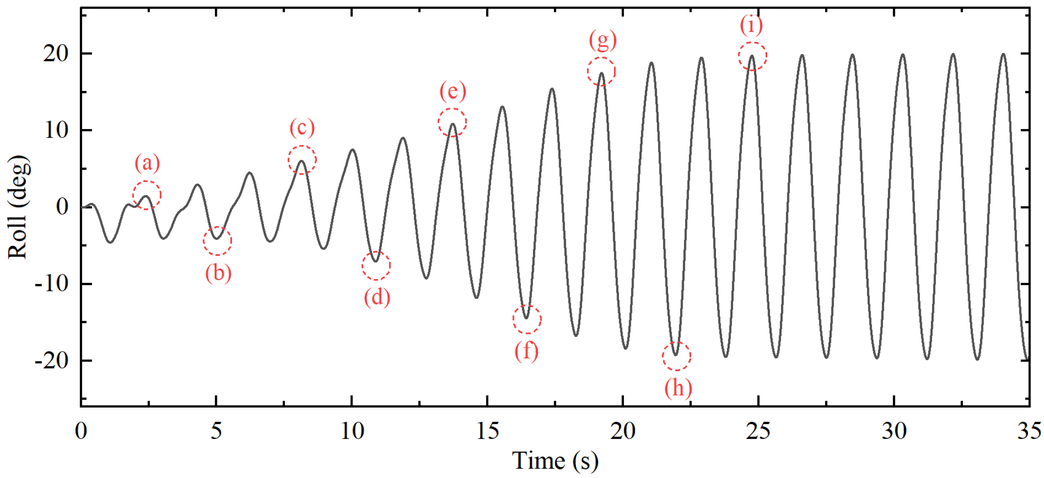

Fig. 16 Representative instants during the development of parametric-roll instability under the 150° oblique head-wave condition

Figures 17 and 18 present the time histories of the roll angle of the KCS hull in oblique head seas (β = 150°) at different model speeds (V_m = 0.5 m/s, 0.6 m/s, 0.7 m/s, and 0.8m/s). Overall, as the model speed increases, the roll response exhibits marked differences in the growth rate of the response amplitude, the final steady-state amplitude, and the oscillation period, indicating that model speed has a pronounced influence on the development of parametric-roll instability in oblique head seas. From the evolution of the roll-response curves, it can be seen that the initial stage responses are relatively similar for all model speeds, all showing a low-amplitude and slowly increasing trend. This suggests that, during this period, wave excitation has not yet induced a pronounced nonlinear response. As time progresses, the influence of model speed on the roll-instability process gradually becomes evident. In particular, for V_m = 0.7 m/s, the roll angle grows more rapidly and reaches a larger steady-state amplitude, exhibiting a stronger parametric-excitation instability feature. After the roll motion enters the quasi-steady stage, the differences among the various speed conditions become more pronounced. The V_m = 0.7 m/s case shows the largest response amplitude and maintains a relatively high roll level even after reaching a stable oscillatory state, indicating that the encounter frequency at this speed is closer to the dominant roll frequency, thereby producing a stronger resonance response. In contrast, although unstable oscillations also occur for V_m = 0.5 m/s and V_m = 0.8 m/s, both the growth rate of the roll amplitude and the final steady-state amplitude are clearly lower than those for V_m = 0.7 m/s, reflecting a reduction in the efficiency of parametric excitation. The response at V_m = 0.6 m/s lies between these two extremes, with a moderate amplitude and growth rate, indicating that a certain excitation effect is still present but that full resonance is not reached. The comparative results indicate that, under oblique head-wave conditions, the influence of model speed on parametric roll exhibits a pronounced nonlinear character. The case of V_m = 0.7 m/s is more likely to trigger a strong resonance response, suggesting that the encounter frequency at this speed is closer to the wave excitation frequency and thus corresponds to the highest risk of roll instability under the present oblique head-wave condition. Compared with the response characteristics in pure head seas, the stronger lateral wave-excitation component and the more complex variation of encounter frequency in oblique head seas make the instability response considerably more selective and sensitive to changes in model speed over a certain range.

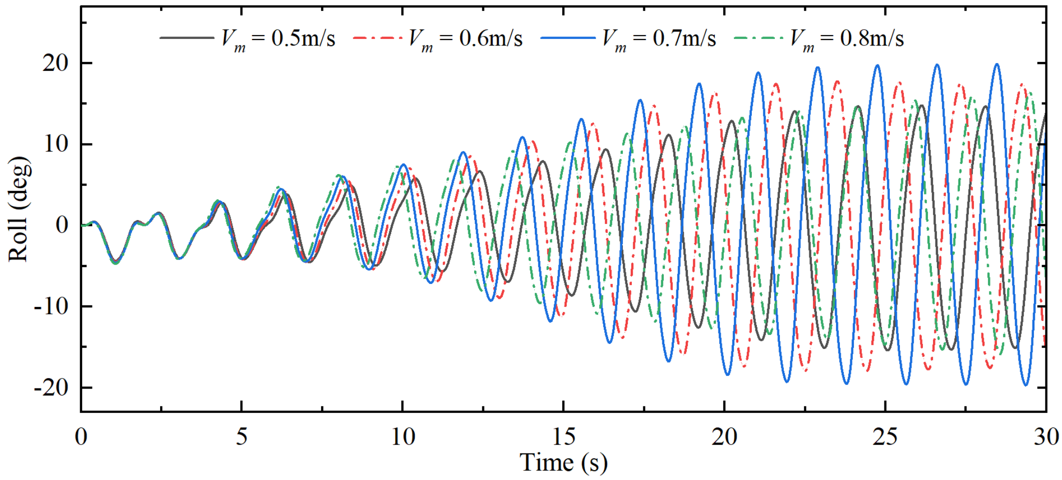

Fig. 17 Time histories of parametric-roll response at different model speeds in oblique head seas (0-30 s)

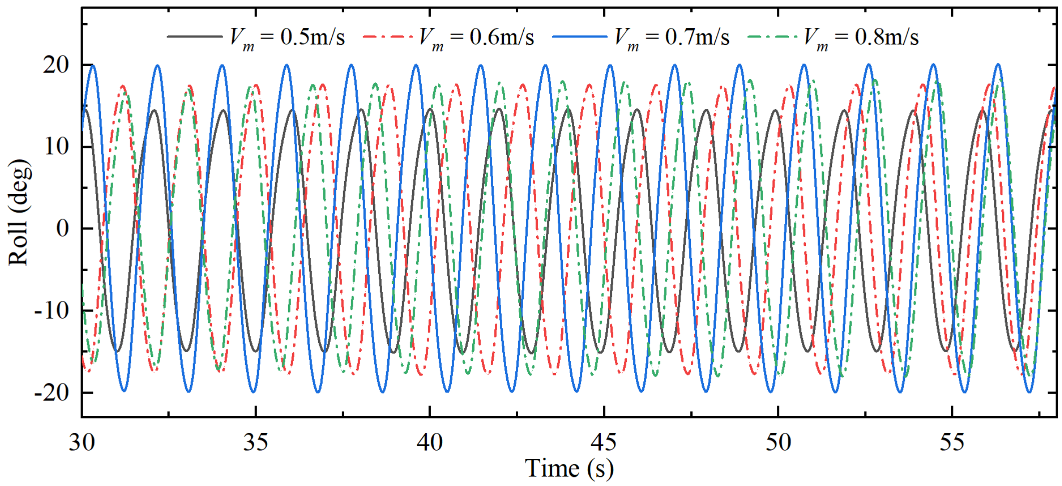

Fig. 18 Time histories of parametric-roll response at different model speeds in oblique head seas (30-58 s).

Figures 19 and 20 present the time histories of the pitch and heave responses of the KCS hull, respectively, under oblique head-wave conditions with a wave-incidence angle of $\beta = 150°$, for different model speeds ($V_m = 0.5$ m/s, 0.6 m/s, 0.7 m/s, and 0.8 m/s). Overall, both the pitch and heave responses exhibit good periodicity for all speed conditions, showing the typical characteristics of linear forced oscillations dominated by wave excitation. In terms of response amplitude and development trend, pitch and heave display some variation with model speed; however, the overall differences remain limited, indicating that these two motion components are relatively insensitive to speed variation. At $V_m = 0.5$ m/s and $V_m = 0.6$ m/s, the pitch amplitude remains relatively small, with the maximum value generally below 3°. The response curves are stable, with regular crests and troughs, indicating that the pitch motion is primarily driven by the periodic wave excitation and is only weakly affected by model speed. As the speed increases to $V_m = 0.7$ m/s, the pitch amplitude increases slightly, with the peak approaching 3.5°. The response curve becomes smoother and more periodic, suggesting that the encounter frequency at this speed is closer to the natural pitch frequency, thereby enhancing the forced-oscillation response. Nevertheless, no pronounced nonlinear amplification is observed in the overall pitch response. This is in sharp contrast to the significant growth of the roll amplitude under the same condition, further indicating that the sensitivity of pitch to model-speed variation is much weaker than that of roll. When the speed is further increased to $V_m = 0.8$ m/s, the pitch amplitude does not continue to increase; instead, it decreases slightly and remains around 3°. At the same time, a slight modulation of the response amplitude appears, manifested as a periodic alternation in crest and trough heights, which can be attributed to the reduced excitation efficiency as the encounter frequency departs from the natural pitch frequency. Overall, the pitch response of the KCS hull in oblique head seas is mainly governed by periodic wave excitation, and its amplitude varies only slightly with model speed, without exhibiting evident nonlinear characteristics. This indicates that, compared with the highly sensitive roll response under the same conditions, pitch has a relatively minor influence on stability safety in oblique head seas, whereas roll remains the dominant motion mode responsible for nonlinear instability.

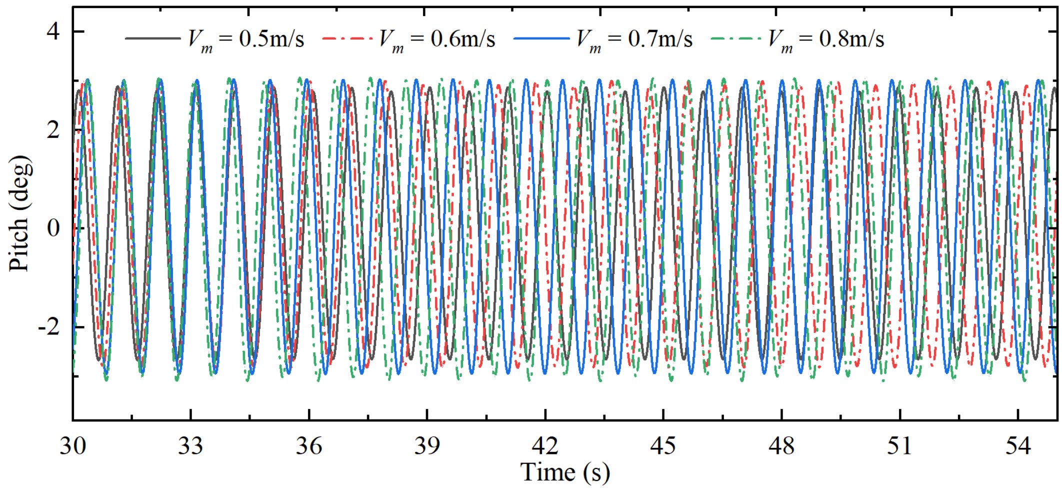

Fig. 19 Time histories of pitch response at different model speeds in oblique head seas(30-55 s)

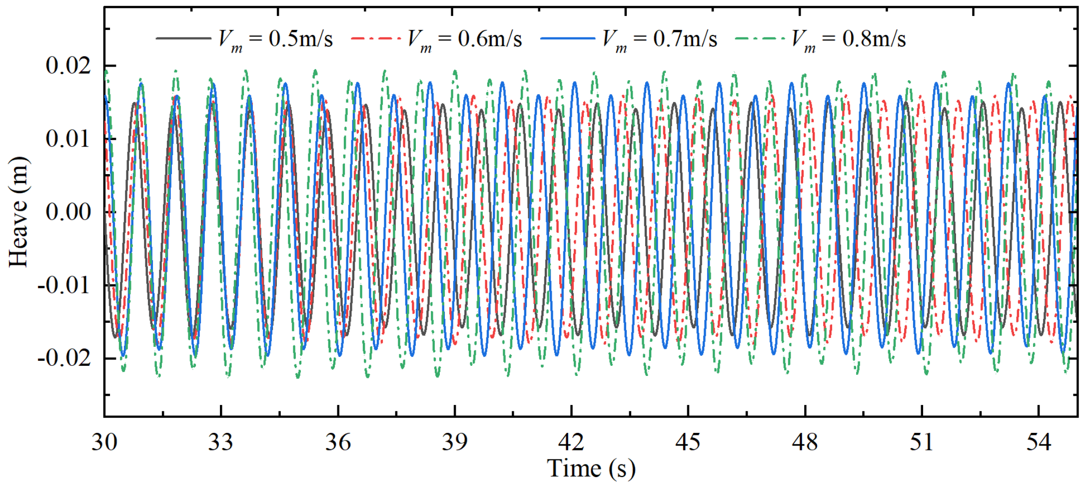

Fig. 20 Time histories of heave response at different model speeds in oblique head seas

To investigate the frequency-domain response characteristics of the KCS hull in oblique head seas, the time histories of roll and pitch motions at different model speeds were transformed into frequency-domain signals using Fourier analysis. The corresponding frequency-domain results are presented in Figure 21. As shown in the figure, the roll response exhibits a pronounced dominant peak at each model speed, with the peak frequency mainly concentrated within the range of 0.5-0.6 Hz. This indicates a clear frequency-selective amplification characteristic of the roll response. Among all cases, the roll amplitude reaches its maximum at V_m = 0.7 m/s, corresponding to a typical parametric-roll instability condition. As the model speed increases from V_m = 0.5 m/s to V_m = 0.7 m/s, the amplitude of the dominant roll-response peak increases markedly. This indicates that, as the encounter frequency gradually approaches twice the dominant frequency of the roll response and enters the frequency range sensitive to parametric roll, the parametric excitation becomes stronger and is more likely to induce nonlinear instability. In addition, the increase in model speed changes the frequency relationship between wave excitation and the roll response. Therefore, the roll-response peak is not fixed at a single frequency, but shifts with the variation in encounter frequency. By contrast, the dominant pitch frequency remains relatively concentrated under different model-speed conditions, mainly within the range of 1.0-1.2 Hz, and its maximum amplitude does not exceed 2.7°, which is substantially smaller than that of roll. This indicates that pitch is not the dominant motion mode in the present oblique-head-sea condition. Moreover, the dominant pitch amplitudes show only limited variation among the different speed cases, suggesting that the pitch response is less sensitive to model-speed variation than the roll response and remains closer to a linear wave-excited response.

From the perspective of frequency-domain energy distribution, the main energy of the roll response is concentrated near half of the encounter frequency, whereas the main energy of the pitch response is concentrated near the encounter frequency. This feature indicates that roll and pitch motions are governed by different dominant excitation mechanisms. The pitch motion is mainly controlled by the direct excitation of the encountered waves, and therefore its dominant response peak is generally consistent with the encounter frequency. In contrast, the dominant peak of the roll response is located near half of the encounter frequency, indicating that the roll amplification exhibits a clear parametric-excitation characteristic. This parametric excitation originates from the periodic variation of the roll restoring characteristics induced by the encountered waves. Its essential frequency condition is manifested as a frequency-doubling relationship between the encounter frequency and the dominant roll-response frequency. Under this condition, the periodic variation of the roll restoring moment can continuously transfer energy into the roll degree of freedom, thereby promoting the growth of the roll response. It should be noted that although the amplitude of pitch motion is much smaller than that of roll motion, its influence during the development of parametric roll cannot be neglected. Pitch motion further changes the instantaneous underwater geometry, waterplane area, wetted-surface distribution, and roll restoring characteristics of the hull, thereby contributing to the periodic variation of the roll restoring moment. Therefore, roll and pitch motions are not independent of each other; rather, they are coupled through the wave-induced variation of ship attitude and restoring characteristics.

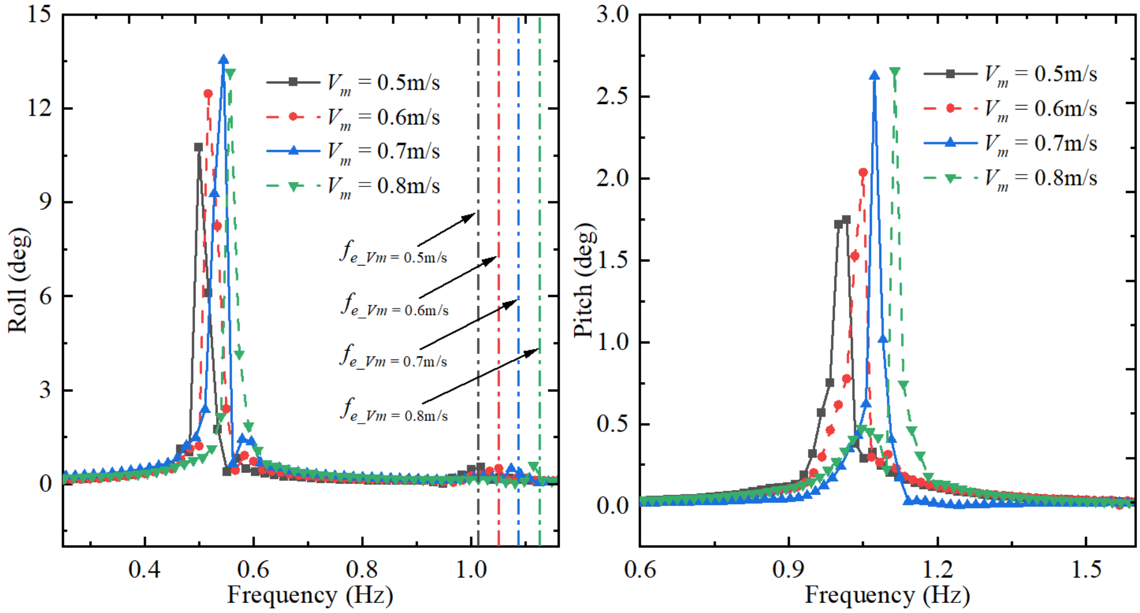

Fig. 21 Frequency-domain responses of roll and pitch motions of the KCS hull at different model speeds

Figure 22 presents the time histories of the heading angle of the KCS hull at different model speeds (V_m = 0.5-0.8 m/s) in oblique head seas with a wave-incidence angle of 150°. Overall, the heading angle exhibits an evident deviation during the initial stage for all speed cases, followed by a decaying oscillatory process, and eventually approaches a dynamically stable state fluctuating around the target heading. In the initial stage, all cases show a relatively large negative heading deviation, with a maximum deviation of approximately 12°. This behavior is mainly attributed to the fact that, at the beginning of the simulation, a steady-state balance has not yet been established between the wave excitation and the ship maneuvering control system. During this stage, the heading response is characterized by the superposition of free decay induced by the initial disturbance and periodic wave forcing, manifested as a rapidly increasing heading error overlaid with slowly decaying oscillations, indicating that the ship is undergoing strong heading disturbances. As time progresses, the heading angles in all speed cases gradually recover toward the target value, accompanied by periodic oscillations whose amplitudes decay with time. Among the cases considered, V_m = 0.7 m/s and V_m = 0.8 m/s show faster convergence and smaller steady-state fluctuations, suggesting that, at higher model speeds, the heading-control system has a stronger capability to suppress wave induced disturbances, thereby providing better course-keeping performance. It is also worth noting that, during the steady-state stage, the heading angle in all speed cases still exhibits small oscillations around the target heading, indicating that wave excitation continues to affect the heading-control system and results in a certain level of persistent heading disturbance. However, this effect is clearly attenuated as the model speed increases, which indirectly demonstrates the positive role of higher forward speed in enhancing rudder effectiveness and improving heading stability.

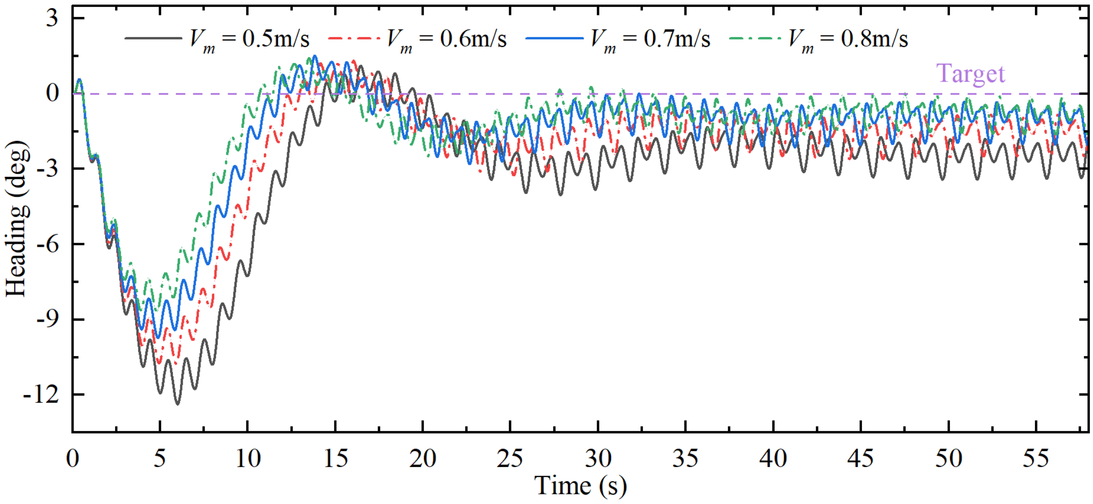

Fig. 22 Time histories of heading angle at different model speeds in oblique head seas

4.3 Analysis of parametric roll instability under different wave directions

Figure 23 illustrates the evolution of the free surface during the development of parametric-roll instability of the KCS hull under the 165° oblique head wave condition. The figure clearly captures the entire process by which the ship's response evolves from an initially stable state to a nonlinear unstable state under this specific wave heading. Overall, the wave crests and troughs on the free surface are distributed obliquely along the wave-propagation direction, resulting in unequal wave action on the port and starboard sides of the hull and thereby creating a sustained lateral excitation environment. In the initial stage of the roll response, the roll angle remains within 3.5°, and the wave pattern is relatively regular, with uniformly spaced crests and troughs, indicating that the wave excitation at this stage is insufficient to trigger instability. As the roll motion enters the development stage, the asymmetry of the free surface on the two sides of the hull becomes increasingly pronounced. In particular, on the positive roll side, the wave crest exhibits a local rise accompanied by evident wave accumulation, whereas on the negative roll side, the trough deepens, leading to a significant increase in wave-height difference between the two sides. This asymmetric excitation drives the roll response into a phase of accelerated growth. Once the roll motion reaches the quasi-steady stage, the roll amplitude approaches 20°, and the free-surface pattern becomes markedly imbalanced.

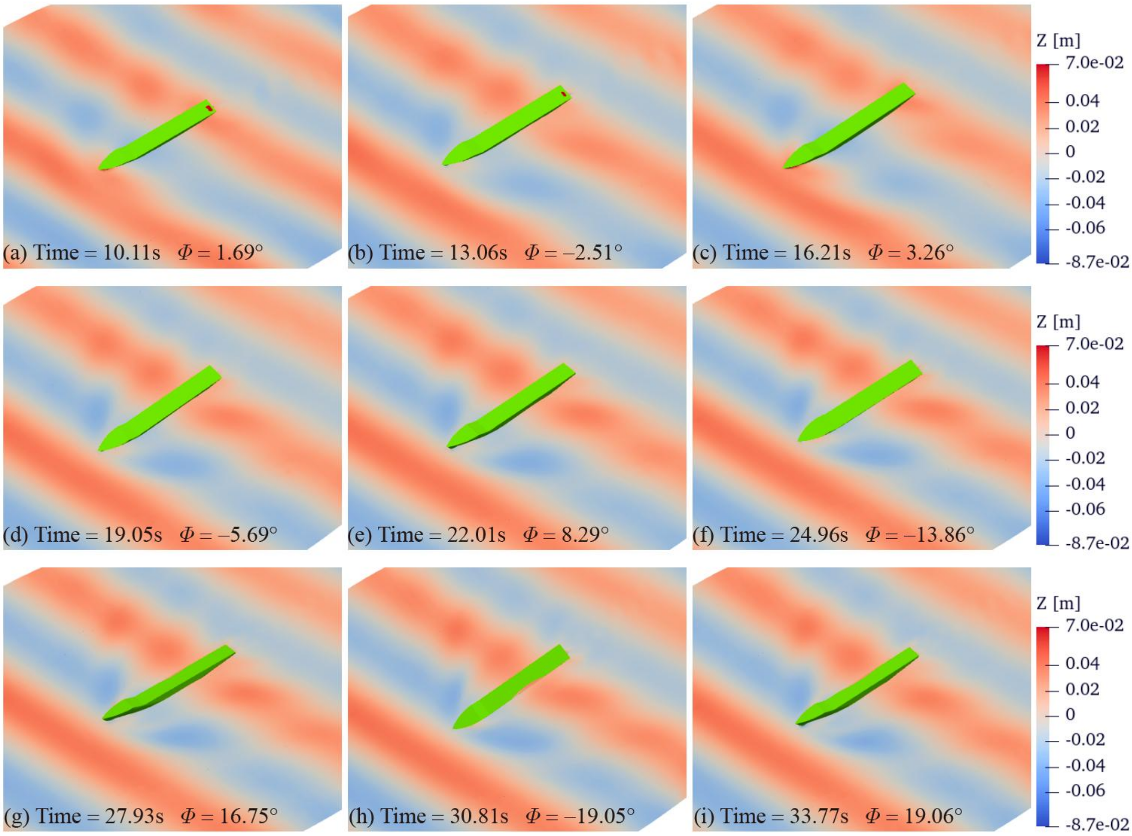

Fig. 23 Evolution of the free surface pattern during parametric roll instability under the 165° oblique head wave condition

Figure 24 presents the time histories of the parametric-roll response of the KCS hull at a model speed of V_m = 0.7 m/s under different wave headings (β = 135°, 150°, 165°, and 180°). Overall, as the wave direction increases from 135° to 180°, the roll response exhibits a progressively stronger nonlinear growth trend. However, clear differences are observed in the growth rate, steady state amplitude, and the time required to reach a stable periodic response, indicating that wave heading has a pronounced influence on the excitation efficiency and development intensity of parametric roll. At β = 135°, the roll response enters the stage of periodic amplification relatively early, but the steady state roll amplitude remains below 12°. The system does not exhibit pronounced nonlinear amplification, suggesting that the wave excitation frequency still deviates to some extent from the roll frequency, thereby limiting the accumulation of nonlinear energy. As the wave heading increases to β = 150°, the roll response begins to amplify significantly after approximately 10s and eventually stabilizes at a relatively large amplitude of about 17°. This indicates that the wave excitation frequency gradually approaches the 2:1 frequency relationship with the roll frequency, thereby strengthening the resonance effect. When the wave heading is further increased to β = 165°, the initial growth rate of the roll response is slightly lower than that for the β = 150° case, but the roll amplitude subsequently undergoes accelerated growth and eventually reaches a steady-state value close to 21°, indicating that the system enters a more strongly nonlinear response regime. This result suggests that, although the initial excitation efficiency at β = 165° is somewhat lower, once resonance is triggered after a longer period of nonlinear energy accumulation, both the response amplitude and its growth rate increase markedly. Under the pure head-sea condition of β = 180°, the roll response shows the most pronounced development trend. Although a certain delay is observed in the initial stage, the roll angle increases rapidly under continuous wave excitation and ultimately reaches a high-amplitude steady state, with a final amplitude close to 23°. This result indicates that, at β = 180°, the encounter frequency is closest to twice the roll frequency of the hull, making it the most favorable condition for strong resonance and consequently large-amplitude nonlinear roll motion. In summary, as the wave heading increases, the wave-incidence direction gradually becomes aligned with the ship's fore–

aft axis, which not only enhances the excitation efficiency but also makes the system more prone to large-amplitude roll responses. Therefore, the head-sea condition can be regarded as the most critical wave-heading range for parametric roll.

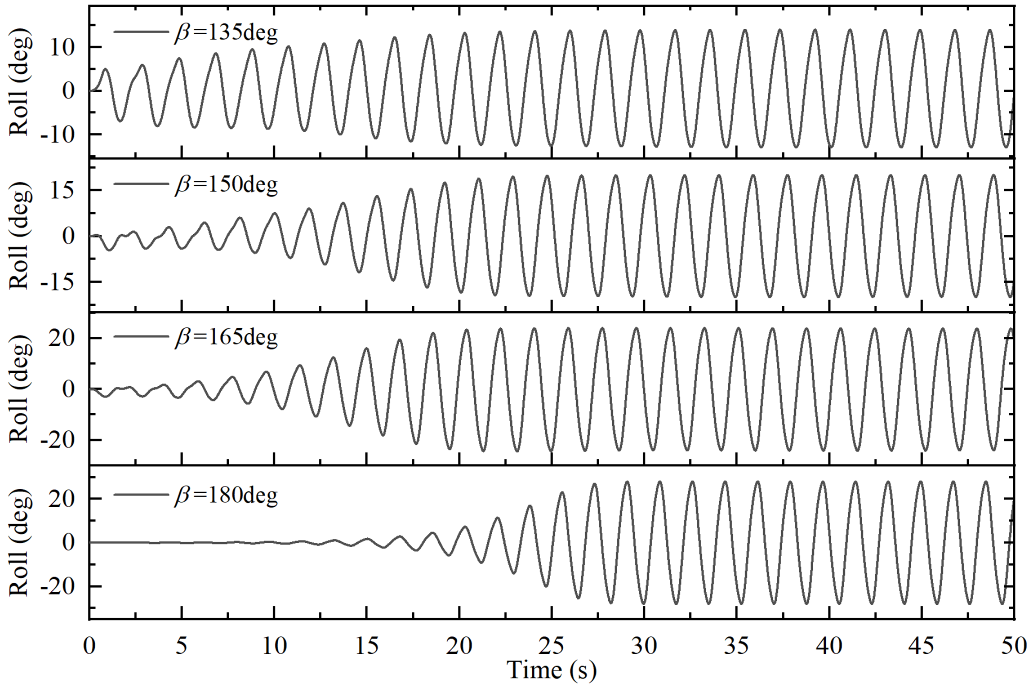

Fig. 24 Comparison of parametric-roll responses under different wave directions

4.4 Study on mitigation and avoidance strategies for parametric roll

4.4.1 Passive roll-reduction method based on a bilge keel

As a typical and widely used roll-reduction device, the bilge keel offers the advantages of structural simplicity, cost effectiveness, and ease of installation [41]. In view of these merits, a bilge keel is selected in this study as the roll reduction device for the KCS container ship. Figures 25 and 26 present the numerical results of the coupled roll, pitch, and heave motions of the KCS hull with and without a bilge keel. The two representative conditions considered are λ/L_{PP} = 1.0, λ/H_W = 0.02, V_m = 0.4 m/s, and λ/L_{PP} = 1.15, λ/H_W = 0.02, V_m = 0.5 m/s respectively. It can be observed that the installation of the bilge keel has a pronounced suppressing effect on the roll response. Without the bilge keel, the roll motion exhibits a clear trend of amplitude growth. By contrast, after the bilge keel is installed, the roll amplitude is significantly reduced and the roll time history becomes much smoother, indicating that the bilge keel effectively delays the development of the nonlinear response. In comparison, the pitch and heave motions are much less sensitive to the bilge keel, and their response trends remain generally unchanged. This indicates that the bilge keel mainly affects the transverse added hydrodynamic characteristics, whereas its influence on the vertical and longitudinal motions is limited. In addition, both the pitch and heave responses exhibit good periodicity and stability, with no obvious sign of instability.

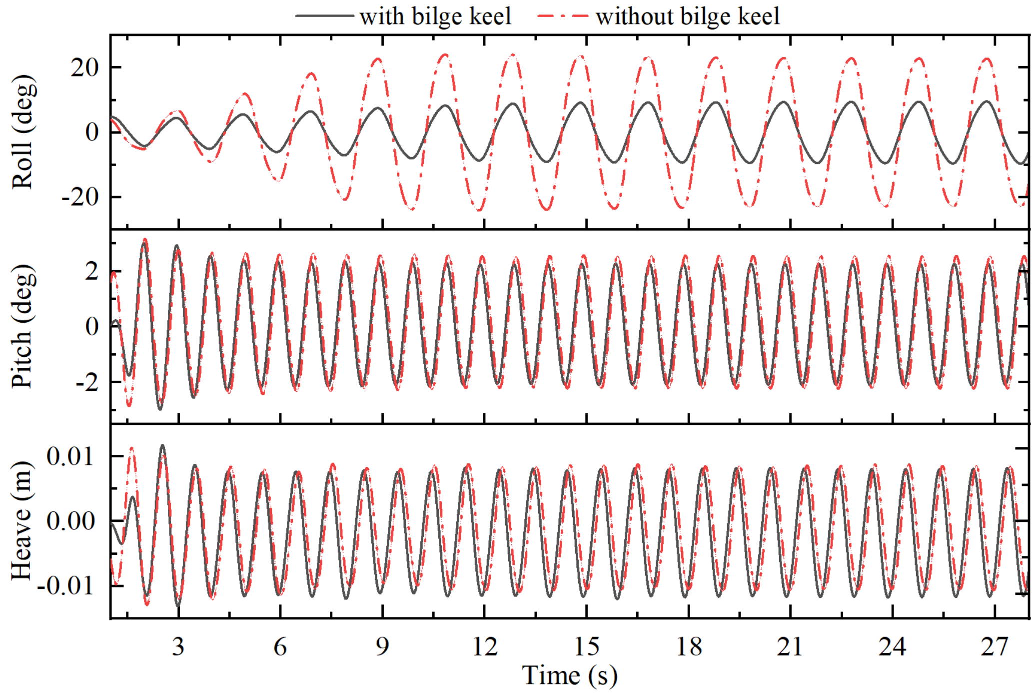

Fig. 25 Comparison of roll, pitch, and heave responses with and without a bilge keel (V_m = 0.4 m/s)

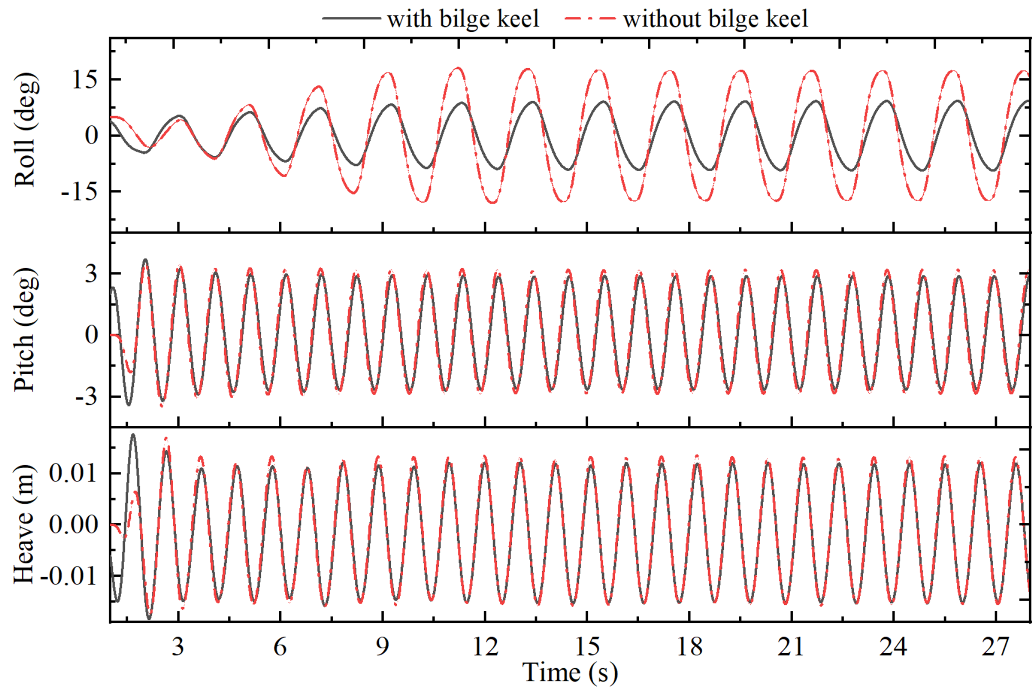

Fig. 26 Comparison of roll, pitch, and heave responses with and without a bilge keel (V_m = 0.5 m/s)

To examine the influence of the bilge keel on wave propagation and free-surface evolution, Figure 27 presents the wave patterns generated during the parametric-roll process of the KCS hull with and without a bilge keel. As shown in the figure, in the absence of a bilge keel, the wave patterns on the two sides of the hull exhibit pronounced asymmetry, accompanied by intense free-surface fluctuations and strong directional disturbances. In contrast, after the bilge keel is installed, the free-surface disturbance becomes considerably smoother and more symmetric, together with a clear reduction in the maximum roll amplitude, as indicated by Φ_{max} in the figure. This change suggests that the installation of the bilge keel alters the local flow structure around the hull and enhances the dissipation of wave-induced energy within the near-field flow, thereby effectively suppressing the continued growth of the roll amplitude.

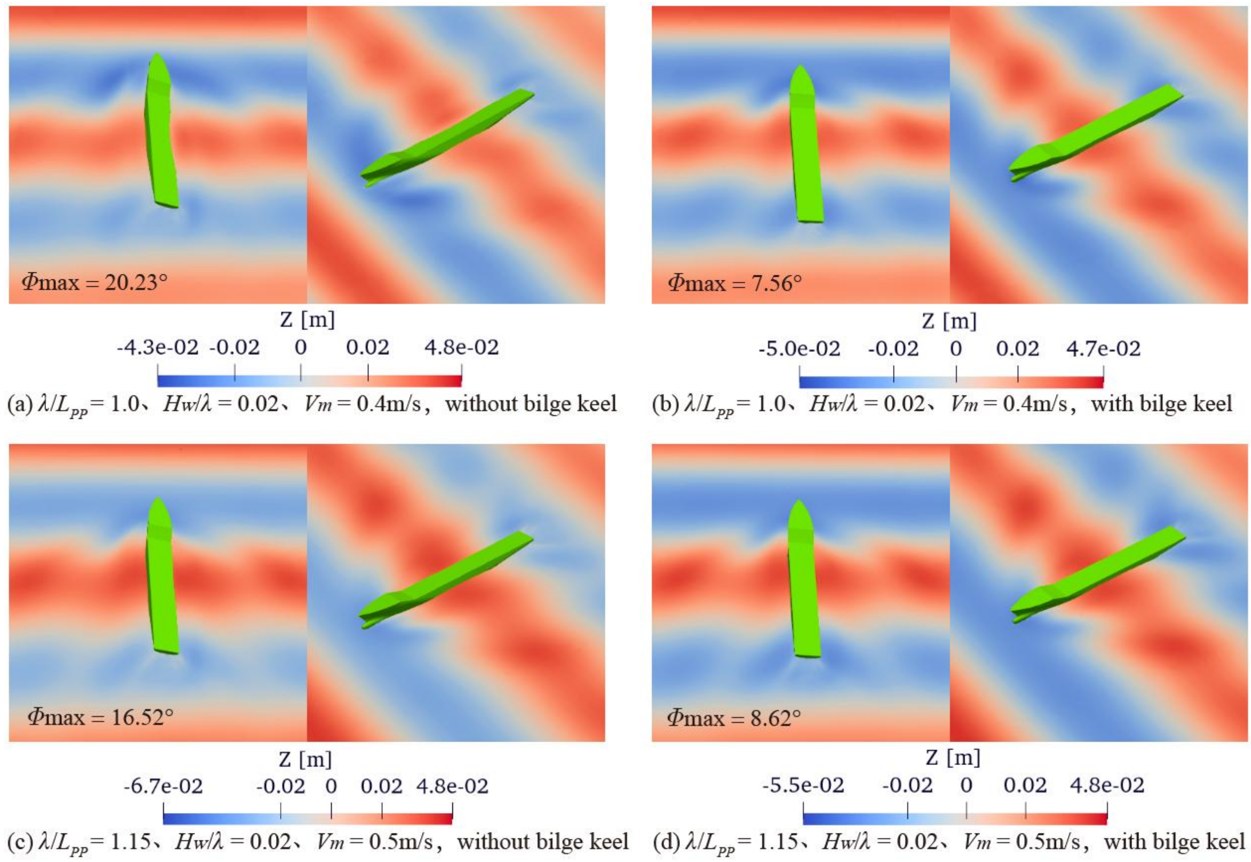

Fig. 27 Wave patterns generated during the parametric-roll motion of the KCS hull with and without a bilge keel

Figure 28 further compares the time histories of the total roll moment for the cases with and without a bilge keel. Without a bilge keel, the total roll moment exhibits pronounced periodic fluctuations, with relatively large positive and negative peaks, indicating a strong unsteady roll-moment input under wave excitation. In contrast, after the bilge keel is installed, the peak values of the total roll moment are significantly reduced, and the fluctuation amplitude is clearly weakened. This demonstrates that the bilge keel effectively reduces the sustained roll-moment input induced by waves. Therefore, the roll-reduction effect of the bilge keel is reflected not only in the reduction of roll amplitude, but also in the attenuation of the roll-moment response. Specifically, the additional damping moment introduced by the bilge keel reduces the possibility of further roll amplification.

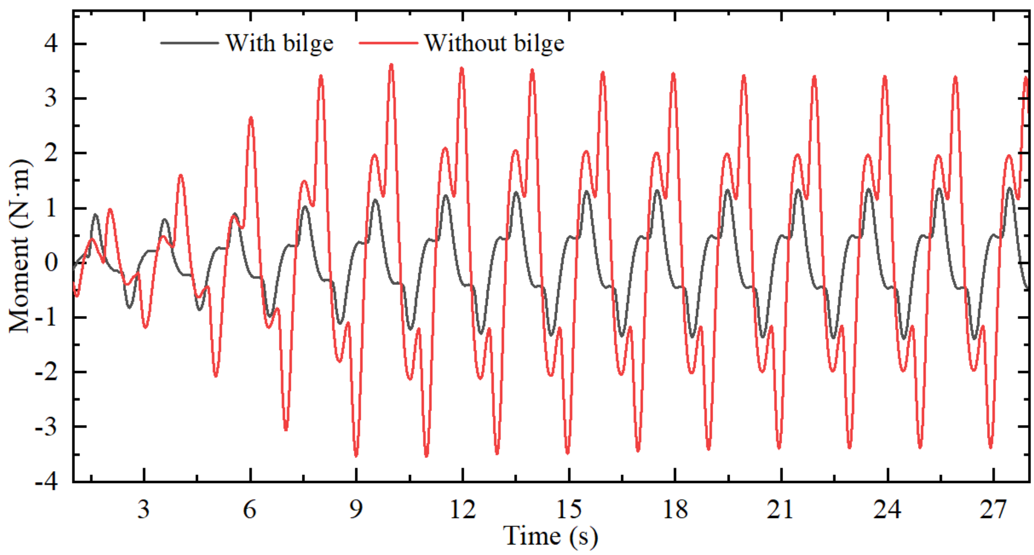

Fig. 28 Comparison of roll-moment time histories for the cases with and without a bilge keel

To further verify the enhancement of roll damping caused by the bilge keel, Figure 29 presents the free-roll decay curves for cases with and without a bilge keel. Under the same initial heel angle, the roll response decays relatively slowly without a bilge keel and still maintains a certain amplitude after several roll cycles. In contrast, with the bilge keel installed, the roll amplitude decreases rapidly within a shorter time, and the decay rate is significantly increased. This indicates that the bilge keel substantially increases the roll damping of the hull, allowing the roll-motion energy to be dissipated more rapidly through viscous and vortex-induced dissipation. The free-roll decay results are consistent with the variation in roll-moment response observed under wave-induced parametric-roll conditions, further confirming that the suppression effect of the bilge keel has a clear damping origin. The above findings are consistent with the conclusions reported by Irkal et al. [21-23] regarding bilge-keel-induced roll damping. By combining free-roll decay experiments, PIV flow-field measurements, and URANS simulations, Irkal et al. systematically investigated the roll damping characteristics of hulls with and without bilge keels. Their results showed that bilge keels can increase roll damping and accelerate the decay of roll motion. In the present study, a similar increase in the roll decay rate is observed after the bilge keel is installed, indicating that the present numerical results are consistent with previous calm-water free-decay studies in terms of the fundamental roll-reduction trend. Furthermore, under oblique head-sea conditions with wave-induced parametric roll, the present simulations show that the bilge keel not only increases calm-water roll damping, but also reduces the peak values of the total roll moment in waves and suppresses the development of large-amplitude parametric roll. This demonstrates that the present study extends the understanding of bilge-keel-induced roll damping from calm-water roll decay to wave-induced parametric-roll instability.

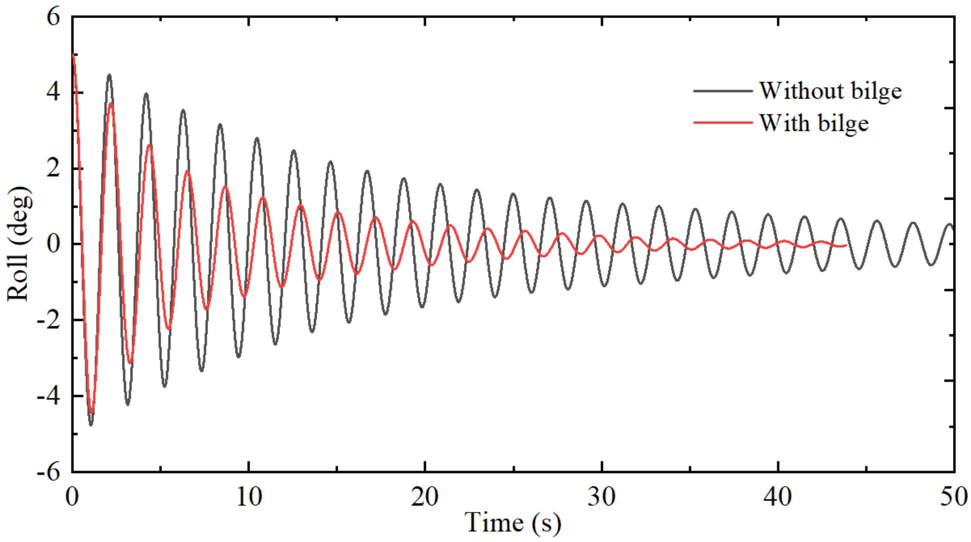

Fig. 29 Free-roll decay curves for the cases with and without a bilge keel

To explain the above roll-reduction effect from the perspective of the local flow field, Figure 30 shows the instantaneous velocity-vector distributions on the midship cross-section of the KCS hull for the cases with and without a bilge keel. Without a bilge keel, the flow near the bilge region is relatively smooth, and no distinct local separation or vortex structures are observed, indicating that the additional energy dissipation in this region is limited. After the bilge keel is installed, clear deflection of the velocity vectors, local flow separation, and vortex structures appear near the bilge-keel tip and its surrounding region. In particular, vortex accumulation and shedding can be observed in the marked region. This is because the bilge keel, as a protruding appendage, enhances the relative motion between the hull and the surrounding fluid during roll oscillation, thereby generating stronger shear flow and unsteady separated flow near the bilge region. This flow process dissipates part of the roll-motion energy and produces an additional damping moment opposite to the roll velocity.

Based on the free-surface patterns, roll-moment responses, free-roll decay curves, and local velocity-vector distributions, it can be concluded that the suppression of parametric roll by the bilge keel is not merely reflected in a reduction in roll amplitude. Instead, it results from several coupled effects, including modification of the local flow structure near the bilge region, enhancement of flow separation and vortex-induced dissipation, increase in roll damping, and attenuation of the unsteady roll-moment input. Compared with previous studies that mainly focused on calm-water free-roll decay and roll damping characteristics, the present results further demonstrate that, under oblique head-sea parametric excitation, the additional damping induced by the bilge keel can reduce the efficiency of sustained wave-energy transfer into the roll degree of freedom. Consequently, the development of large-amplitude parametric roll is effectively suppressed, and the transverse stability of the ship under wave excitation is improved.

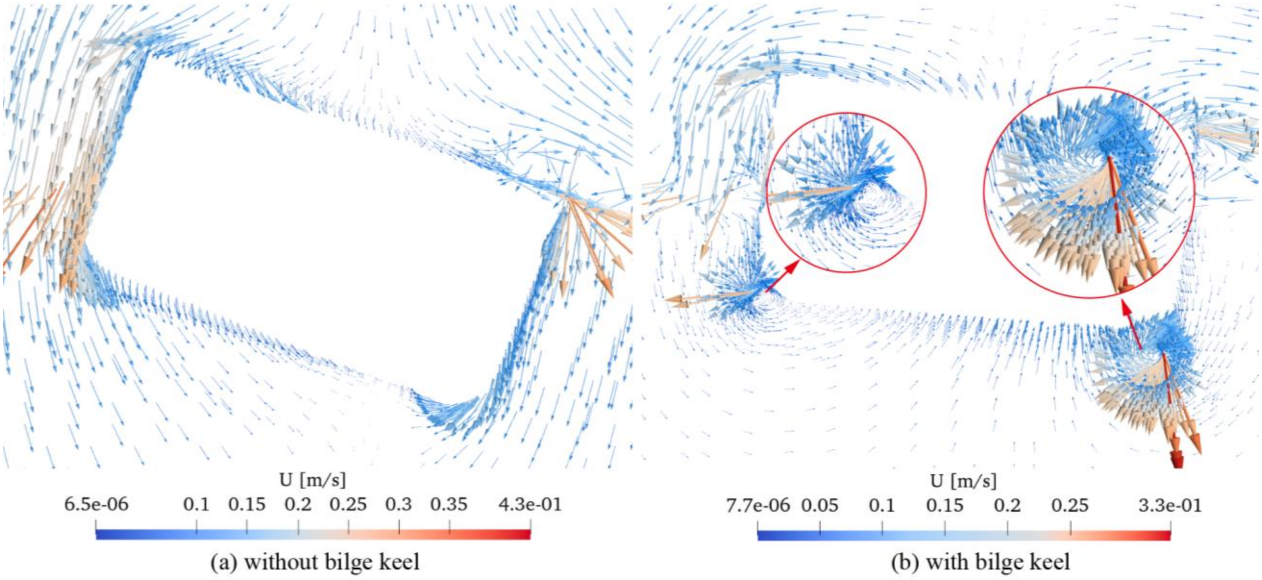

Fig. 30 Velocity-vector distributions at the midship transverse section of the KCS hull

4.4.2 Active avoidance strategy based on speed control

In a typical parametric roll scenario, when the encounter frequency approaches twice the roll frequency of the ship, the system is highly susceptible to entering the resonance region, thereby triggering rapid growth of the roll response. To address this issue, adjusting the model speed to alter the encounter frequency and thus drive the system away from the resonance region constitutes an active avoidance strategy of practical relevance. This approach does not require additional structural devices and offers good operability and applicability under different sea states and operating conditions. To further investigate the influence of speed variation on the roll response, two controlled scenarios, namely acceleration and deceleration, are designed in this study. Unsteady CFD simulations are then performed to systematically evaluate the response characteristics of roll amplitude and instability tendency during the process of encounter-frequency variation.

Figures 31 and 32 present the time histories of the roll response and model speed during the acceleration process for the $\beta = 150°$ and $\beta = 165°$ conditions, respectively. In the initial stage, the ship remains within the roll-resonance region under both wave headings, and the roll response continues to grow with time until it gradually reaches a saturated state, exhibiting the typical characteristics of parametric roll. At Time = 60 s, acceleration control is implemented through the maneuvering-control module, causing a rapid increase in model speed and consequently altering the relative motion between the ship and the waves. During this process, the encounter frequency gradually departs from its frequency-doubling relationship with the roll frequency, so that the system progressively moves out of the resonance region, and the roll response correspondingly exhibits a clear decay trend. Although the overall response trends are similar under the two conditions, significant differences are observed in the decay rate of the roll amplitude and the residual response. Compared with the $\beta = 165°$case, the decay of roll amplitude in the $\beta = 150°$ case is noticeably slower and is accompanied by stronger short-term nonlinear residual oscillations. The primary reason is that, under $\beta = 150°$, the angle between the wave-propagation direction and the ship longitudinal axis is larger, resulting in a stronger lateral excitation component and hence a greater effective excitation intensity in the roll direction. As a result, even after the ship has moved out of the resonance region during acceleration, the lateral disturbance still sustains the pre-existing roll response to some extent. By contrast, under the $\beta = 165°$condition, the wave propagation direction is more closely aligned with the ship longitudinal axis, and the encounter frequency changes more rapidly during acceleration, enabling the system to leave the resonance region more quickly and thereby promoting a more pronounced decay of the roll response. In comparison, under $\beta = 150°$, the encounter frequency is less sensitive to the speed variation, which delays the departure from the resonance region and consequently prolongs the decay process of the roll amplitude.

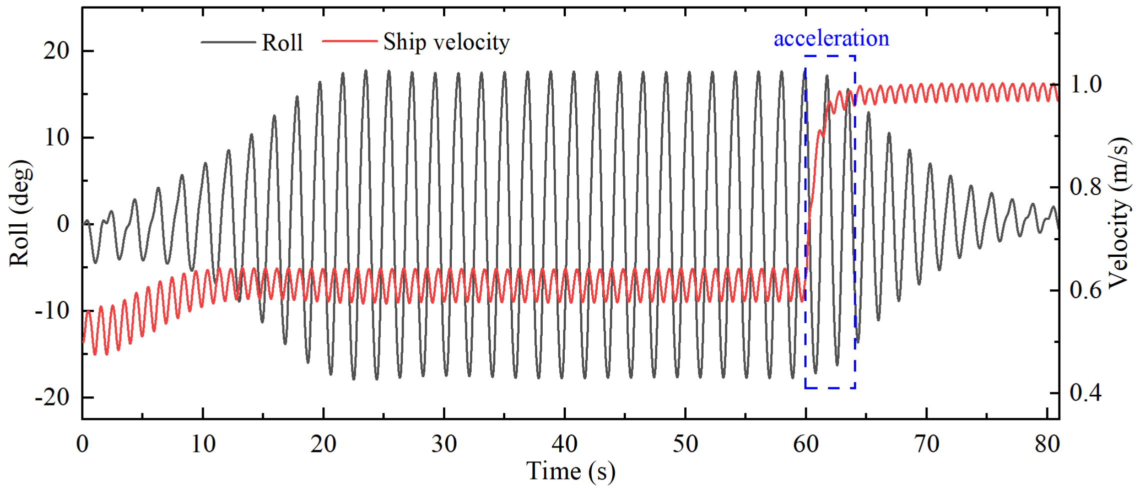

Fig. 31 Time histories of roll response and model speed during acceleration under the $\beta = 150°$ condition

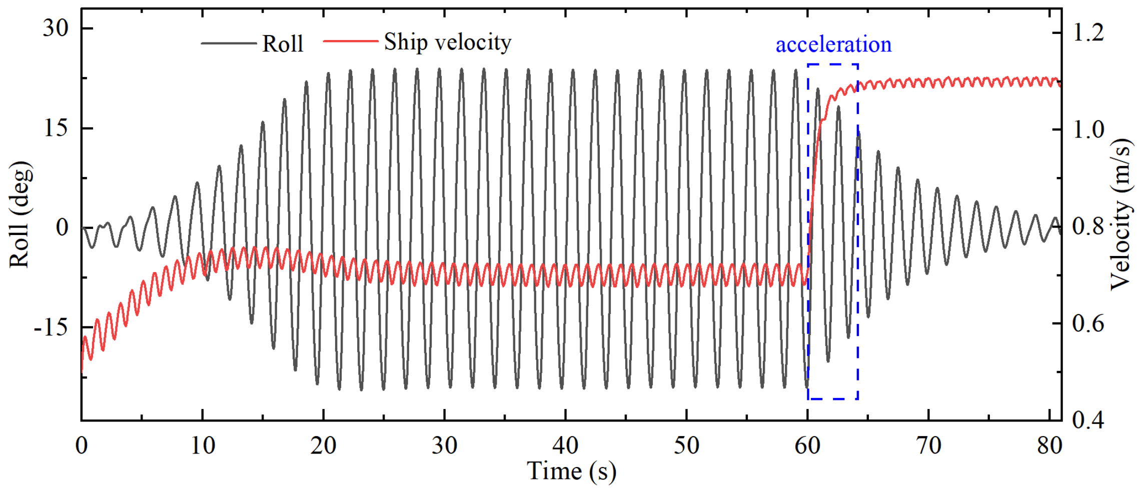

Fig. 32 Time histories of roll response and model speed during acceleration under the $\beta = 165°$ condition

Figures 33 and 34 show the time histories of roll motion and model speed during the deceleration process under the $\beta = 150°$ and $\beta = 165°$ conditions, respectively. It can be observed that, before Time = 60 s, the ship exhibits a clear parametric-roll response under both wave headings, with the roll amplitude gradually increasing and approaching a saturated state. At Time = 60 s, active deceleration control is applied through the control system, resulting in a rapid decrease in model speed. Consequently, the encounter relationship between the ship and the incident waves changes, and the roll response shifts from a continuously amplified state to an unsteady adjustment process. For the $\beta = 165°$ condition, a pronounced transient increase in roll angle occurs during the initial stage of deceleration, with the maximum positive and negative roll angles reaching approximately 28.5° and -25.6°, respectively. This indicates that the deceleration operation does not immediately attenuate the roll response. Instead, the rapid variation in model speed introduces a strong transient disturbance, causing the roll motion to be further amplified within a short period. Subsequently, as the model speed continues to decrease, the ship gradually moves away from the original parametric-roll-sensitive region, and the roll amplitude decreases rapidly, eventually maintaining only small-amplitude oscillations. For the $\beta = 150°$ condition, a transient increase in roll angle is also observed after deceleration, but the corresponding amplitude is relatively smaller. The maximum positive and negative roll angles are approximately 21.6° and -19.7°, respectively. After the deceleration process is completed, the roll response also gradually decays and approaches a small-amplitude oscillatory state. These results indicate that deceleration control can eventually move the ship away from the original parametric-roll-sensitive region and promote the decay of the roll response. However, during the initial stage of deceleration, it may induce a pronounced transient amplification of roll motion. This phenomenon is more evident under the oblique head-sea condition closer to head seas. Unlike the acceleration process, in which the roll response is gradually weakened, the unstable response induced by deceleration is more abrupt and severe. Therefore, in active avoidance strategies based on speed control, deceleration operations may involve a higher risk of transient roll amplification and should be treated with particular caution in ship operation.

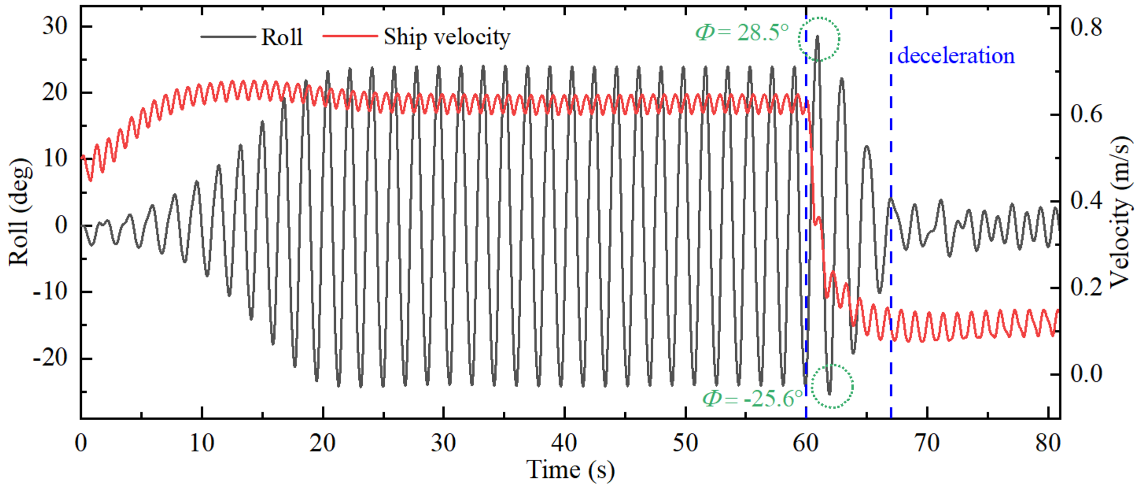

Fig. 33 Time histories of roll response and model speed during deceleration under the β = 165° condition

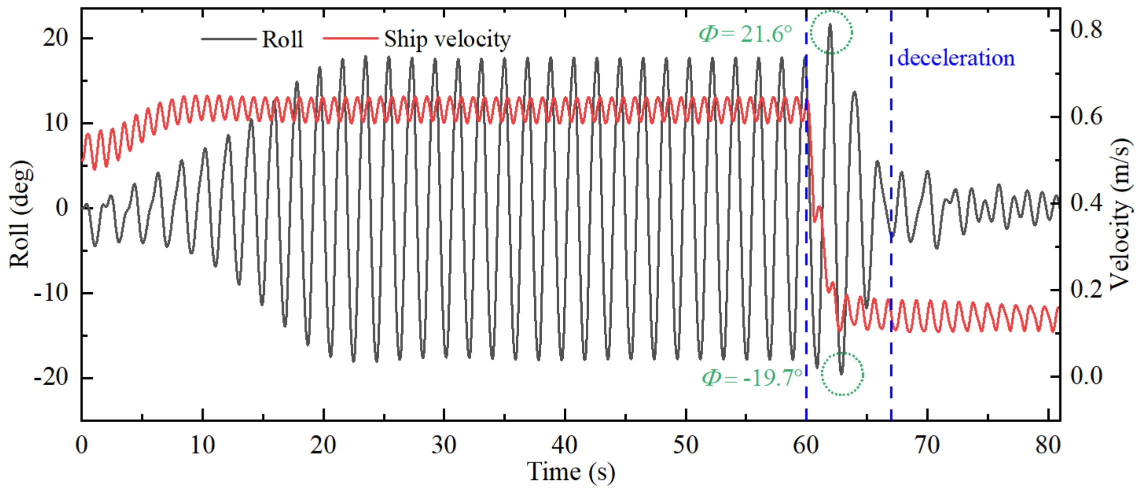

Fig. 34 Time histories of roll response and model speed during deceleration under the β = 150° condition

Figures 35 and 36 show the time histories of the total roll moment during the acceleration and deceleration processes under the wave-heading conditions of β = 150° and β = 165°, respectively. It can be observed that the roll-moment responses begin to differ rapidly after the speed adjustment is initiated. In the deceleration cases, relatively large transient roll-moment peaks are more likely to occur during the initial stage, whereas in the acceleration cases, the roll-moment oscillations persist for a longer duration. This indicates that speed variation not only changes the relationship between the encounter frequency and the roll response, but also modifies the periodic variation characteristics of the roll restoring moment in waves, thereby affecting the energy input process associated with parametric roll. A further comparison between different wave-heading conditions shows that, under the β = 150° condition, the larger angle between the wave propagation direction and the ship's longitudinal axis leads to a more pronounced direct roll-excitation component induced by oblique waves. This component may continue to contribute to roll-moment fluctuations even after the ship accelerates away from the parametric-roll-sensitive region, thereby leaving a certain level of residual roll oscillation. From the perspective of active avoidance, acceleration control mainly increases the model speed so that the encounter frequency gradually moves away from the parametric-roll-sensitive region. This weakens the sustained roll-moment input and promotes the decay of the roll response. In contrast, deceleration control may induce a relatively large transient roll moment during the initial stage, causing the roll angle to increase further within a short period.

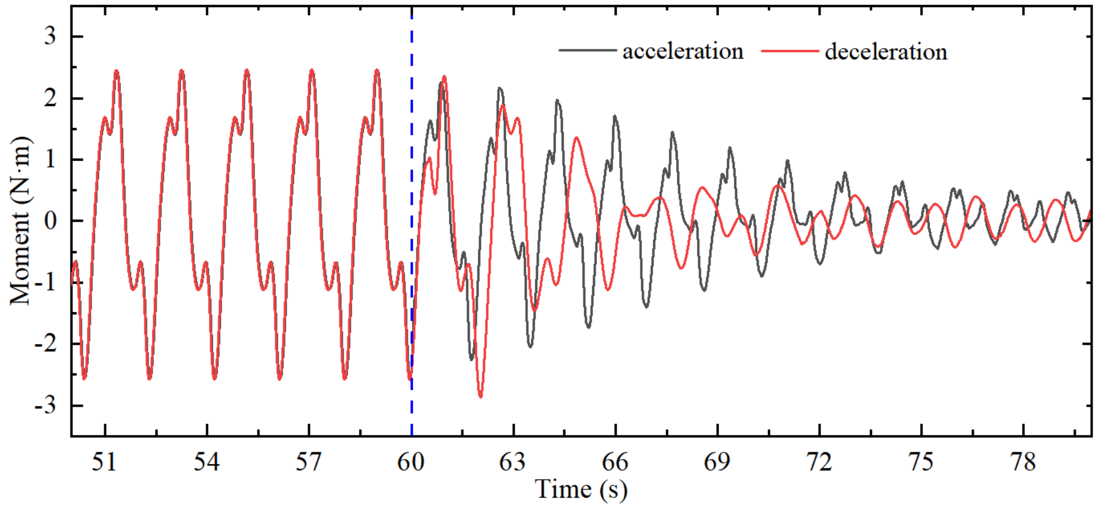

Fig. 35 Comparison of roll moments during acceleration and deceleration under the 150° wave-heading condition

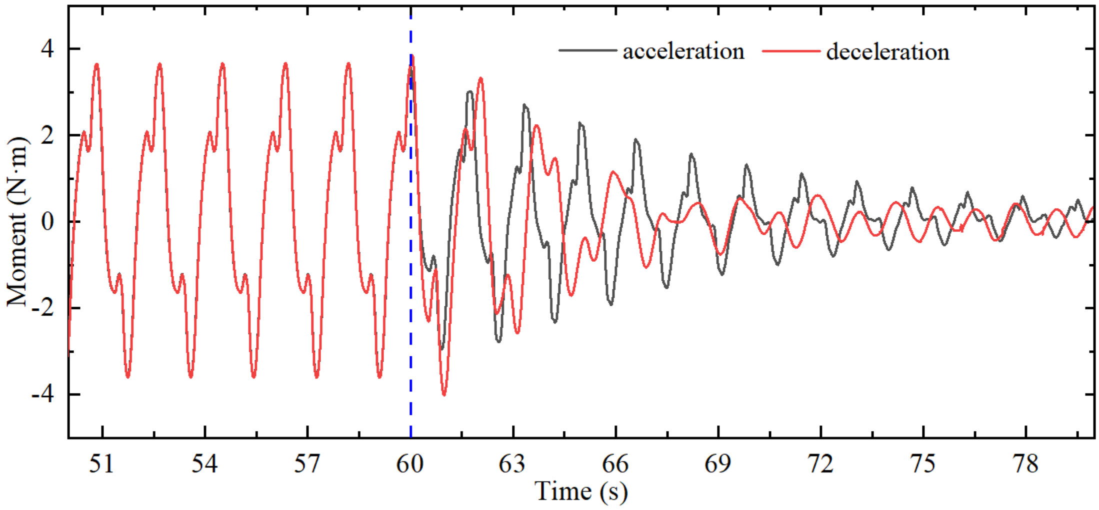

Fig. 36 Comparison of roll moments during acceleration and deceleration under the 165° wave-heading condition

Based on the above analysis of acceleration and deceleration control, the occurrence and non-occurrence of parametric roll under different wave-heading and model-speed conditions were further summarized to determine the minimum model speed required to avoid parametric roll under the wave condition considered in this study. Figure 37 shows the occurrence states of parametric roll for different combinations of wave heading and model speed, where the black circles indicate the occurrence of parametric roll and the red triangles indicate no parametric roll. As shown in Figure 37, the occurrence of parametric roll is closely related to both wave heading and model speed. Under the β = 150° condition, parametric roll occurs over the range of V_m = 0.5-0.8 m/s. When the model speed is increased to V_m = 0.85 m/s, no sustained growth of the roll amplitude is observed, indicating that parametric roll is avoided. Therefore, the minimum model speed required to avoid parametric roll under this wave heading is approximately 0.85 m/s. Under the β = 165° condition, parametric roll occurs within the range of V_m = 0.7-0.85 m/s, whereas no sustained parametric-roll response is observed when the model speed increases to V_m = 0.90 m/s. Thus, the corresponding minimum avoidance speed is approximately 0.90 m/s. For the head-sea condition of β = 180°, the speed range associated with parametric roll shifts further toward higher model speeds. Parametric roll still occurs at V_m = 0.95 m/s, while the roll response remains within a small-amplitude range at V_m = 1.0 m/s. Therefore, the minimum avoidance speed under the head-sea condition is approximately 1.0 m/s. These results indicate that, under the wave condition considered in this study, the minimum model speed required to avoid parametric roll increases as the wave heading approaches head seas. From the perspective of operational guidance, Figure 37 can be used to provide a heading-dependent reference for parametric-roll avoidance under a specific wave condition. For the present wave condition, the minimum model speeds required to avoid parametric roll under β = 150°, β = 165°, and β = 180° are approximately 0.85, 0.90, and 1.0 m/s, respectively. It should be noted that these avoidance speeds were obtained from CFD simulations under the specific wavelength, wave height, and model-scale conditions considered in this study, and should not be directly interpreted as general operational limits applicable to all sea states. The main significance of these results is that CFD can not only identify the occurrence of parametric roll, but can also be further used to construct heading-dependent operational guidance for parametric-roll avoidance, thereby providing a reference for speed adjustment and instability avoidance under specific sea conditions.

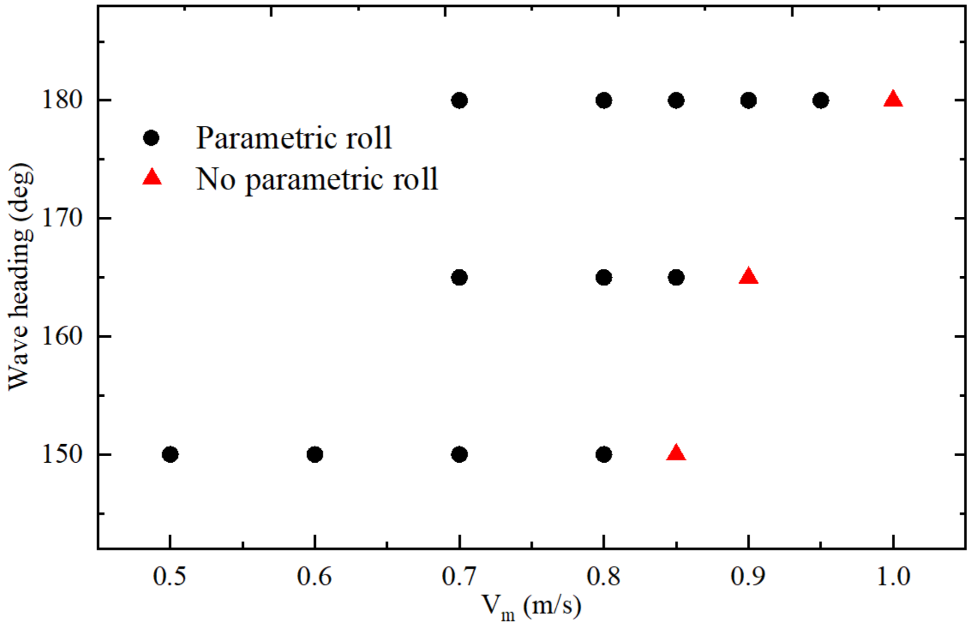

Fig. 37. Parametric-roll occurrence under different wave-heading conditions

5. Conclusion

This study focuses on parametric roll instability in oblique head seas. A six-degree-of-freedom numerical model that accounts for the coupled effects of the hull, rudder, and propeller is established within a CFD framework, and parametric roll responses under regular wave conditions are investigated. The influences of model speed and wave heading on the instability characteristics of the KCS hull are systematically examined. In addition, two representative mitigation and avoidance strategies are explored from both passive and active perspectives, namely the bilge keel and speed control. The main conclusions are summarized as follows:

(1) Under oblique head-wave conditions, when the model speed lies near the upper or lower bounds of the resonance region, the efficiency of roll excitation decreases markedly, indicating that the parametric excitation is highly selective and sensitive to speed variation in oblique waves.

(2) A higher model speed helps maintain heading stability and a nearly constant wave-incidence angle, thereby reinforcing the periodic roll excitation. In contrast, at lower speeds, heading deviation tends to disrupt the coupling between wave excitation and restoring characteristics, leading to a reduction in roll-excitation effectiveness.

(3) As the wave direction increases from 135° to 180°, the parametric-roll response exhibits both amplitude amplification and enhanced nonlinearity. In particular, the β = 165° and β = 180° cases are the most prone to strong resonance, showing larger steady-state roll amplitudes and more pronounced asymmetric free-surface disturbances. This indicates that the head-sea range is the most critical wave-heading region for parametric roll, within which the risk of instability increases significantly.

(4) The bilge keel effectively suppresses the amplitude growth of parametric roll by increasing the additional damping. Under resonant conditions, the installation of a bilge keel significantly reduces the nonlinear growth rate of the roll response and delays the onset of instability. Meanwhile, the bilge keel induces vortex structures that enhance local kinetic-energy dissipation in the flow field and weaken the effective wave-energy input, thereby improving the transverse motion stability of the ship in waves.

(5) The active avoidance strategy based on speed control can effectively reduce the nonlinear response by adjusting the encounter frequency and thereby steering the system away from the roll resonance region. Under acceleration, the roll amplitude gradually decays as the system moves out of the resonance zone, resulting in a pronounced roll-reduction effect. By contrast, during deceleration, a secondary excitation phenomenon may occur in the initial stage, causing a sudden increase in roll amplitude and amplifying the nonlinear response. Therefore, acceleration control is more effective and practical for roll mitigation, whereas deceleration requires caution because of its potential instability risk.

ACKNOWLEDGMENTS

The authors gratefully acknowledge the support from the National Natural Science Foundation of China (Grant Nos. 51779135 and 51009087), Shanghai Natural Science Foundation of China (project approval number: 14ZR1419500), and Shandong Provincial Natural Science Foundation (No. ZR2025QC578).

REFERENCES

[1] Hu, K., Wang, R., Ma, S., Duan, W., Xu, W., Deng, R. 2017. Numerical modelling and study of parametric rolling for C11 containership in regular head seas using consistent strip theory. *Brodogradnja*, 68(3), 135-156. https://doi.org/10.21278/brod68309

[2] Imo. 2023. Explanatory Notes to the Interim Guidelines on the Second Generation Intact Stability Criteria. *MSC.1/Circ.1652*, London, United Kingdom. https://puc.overheid.nl/nsi/doc/PUC_743708_14/1/

[3] Kerwin, J. 1955. Notes on rolling in longitudinal waves. *International Shipbuilding Progress*, 2(16), 597-614.

[4] Bulian, G. 2004. Approximate analytical response curve for a parametrically excited highly nonlinear 1-DOF system with an application to ship roll motion prediction. *Nonlinear analysis: real world applications*, 5(4), 725-748. https://doi.org/10.1016/j.nonrwa.2004.03.002

[5] Song, K., Kim, Y., Song, K. H., Kim, Y., 2011. Quantitative analysis of parametric roll and operational guidance. *Proceedings of the 12th International Ship Stability Workshop*, 12-15 June, Washington DC, USA.

[6] Umeda, N., Hashimoto, H., Vassalos, D., Urano, S., Okou, K. 2004. Nonlinear dynamics on parametric roll resonance with realistic numerical modelling. *International Shipbuilding Progress*, 51(2-3), 205-220. https://doi.org/10.3233/SHP-2004-51.2_3_6

[7] Hashimoto, H., Umeda, N. 2004. Nonlinear analysis of parametric rolling in longitudinal and quartering seas with realistic modeling of roll-restoring moment. *Journal of Marine Science and Technology*, 9, 117-126. https://doi.org/10.1007/s00773-004-0184-8

[8] Schrøter, C., Lützen, M., Erichsen, H., Jensen, J. J., Kristensen, H. O., Lauridsen, P. H., Tunccan, O., Baltsersen, J. P., 2017. Sample applications of the second generation intact stability criteria–robustness and consistency analysis. *16th International ship stability workshop*, 20 September, Belgrade, Serbia.

[9] Sakai, M., Umeda, N., Maki, A. 2019. Encounter frequency effect on the simplified design criteria against parametric roll. *Ocean Engineering*, 182, 21-27. https://doi.org/10.1016/j.oceaneng.2019.04.061

[10] Marlantes, K. E., Kim, S., Hurt, L. A. 2021. Implementation of the IMO second generation intact stability guidelines. *Journal of Marine Science and Engineering*, 10(1), 41. https://doi.org/10.3390/jmse10010041

[11] Loya, K., Tallapragada, P. 2023. Parametric roll oscillations of a hydrodynamic Chaplygin sleigh. *Nonlinear Dynamics*, 111(22), 20699-20713. https://doi.org/10.1007/s11071-023-08960-3

[12] Hashimoto, H., Furusho, K. 2022. Influence of sea areas and season in navigation on the ship vulnerability to the parametric rolling failure mode. *Ocean Engineering*, 266, 112714. https://doi.org/10.1016/j.oceaneng.2022.112714

[13] Somayajula, A., Falzarano, J., Lutes, L. 2019. An efficient assessment of vulnerability of a ship to parametric roll in irregular seas using first passage statistics. *Probabilistic Engineering Mechanics*, 58, 102998. https://doi.org/10.1016/j.probengmech.2019.102998

[14] Somayajula, A., Falzarano, J. 2019. Parametric roll vulnerability of ships using Markov and Melnikov approaches. *Nonlinear Dynamics*, 97(4), 1977-2001. https://doi.org/10.1007/s11071-019-05090-7

[15] E Silva, S. R., Santos, T., Soares, C. G., 2003. Time Domain Simulations of a Coupled Parametrically Excited Roll Response in Regular and Irregular Head Seas. *8th International Conference on the Stability of Ships and Ocean Vehicles*, 15-19 September, Madrid, Spain.

[16] Bulian, G. 2005. Nonlinear parametric rolling in regular waves—a general procedure for the analytical approximation of the GZ curve and its use in time domain simulations. *Ocean Engineering*, 32(3-4), 309-330. https://doi.org/10.1016/j.oceaneng.2004.08.008

[17] Neves, M. A., Pérez, N., Lorca, O., 2002. Experimental analysis on parametric resonance for two fishing vessels in head seas. *Proceedings of the 6th international ship stability workshop*, 13-16 October, Glen Cove, New York, USA.

[18] Neves, M. A., Rodriguez, C. A. 2006. On unstable ship motions resulting from strong non-linear coupling. *Ocean Engineering*, 33(14-15), 1853-1883. https://doi.org/10.1016/j.oceaneng.2005.11.009

[19] Rodriguez, C., Holden, C., Perez, T., Drummen, I., Neves, M. D. a. S., Fossen, T., 2007. Validation of a container ship model for parametric rolling. *Proceedings of the 9th International Ship Stability Workshop*, 30-31 August, Hamburg, Germany. https://doi.org/https://eprints.qut.edu.au/78291/

[20] Holden, C., Galeazzi, R., Rodríguez, C., Perez, T., Fossen, T. I., Blanke, M., De Almeida Santos Neves, M. 2007. Nonlinear container ship model for the study of parametric roll resonance. *Modeling, identification and control*, 28(4), 87-103. https://doi.org/10.4173/mic.2007.4.1

[21] Irkal, M. a. R., Nallayarasu, S., Bhattacharyya, S. K. 2016. CFD approach to roll damping of ship with bilge keel with experimental validation. *Applied Ocean Research*, 55, 1-17. https://doi.org/10.1016/j.apor.2015.11.008

[22] Irkal, M. A., Nallayarasu, S., Bhattacharyya, S., 2019. Effect of forward speed on roll damping of a container ship using URANS simulations. *Proceedings of the Fourth International Conference in Ocean Engineering* (ICOE2018), 18-21 February, IIT Madras, Chennai, India. https://doi.org/10.1007/978-981-13-3119-0_12

[23] Irkal, M. a. R., Nallayarasu, S., Bhattacharyya, S. K. 2019. Numerical prediction of roll damping of ships with and without bilge keel. *Ocean Engineering*, 179, 226-245. https://doi.org/10.1016/j.oceaneng.2019.03.027

[24] Zhou, Y. 2016. Study on Parametric Rolling Prediction of Full Scale Container Ship Based on A Hybrid Method. *Doctoral Dissertation*, Shanghai Jiao Tong University, Shanghai, P.R.China.

[25] Zhou, Y. 2019. Further validation study of hybrid prediction method of parametric roll. *Ocean Engineering*, 186, 106103. https://doi.org/10.1016/j.oceaneng.2019.06.008

[26] Ma, S., Ge, W.-P., Ertekin, R., He, Q., Duan, W.-Y. 2018. Experimental and numerical investigations of ship parametric rolling in regular head waves. *China Ocean Engineering*, 32(4), 431-442. https://doi.org/10.1007/s13344-018-0045-6

[27] Liu, L., Feng, D., Wang, X., Zhang, Z., Yu, J., Chen, M. 2022. Numerical study on the effect of sloshing on ship parametric roll. *Ocean Engineering*, 247, 110612. https://doi.org/10.1016/j.oceaneng.2022.110612

[28] Liu, L., Dong, K., Chen, J., Chen, M., Wang, X. 2022. Numerical Study on Parametric Roll of Full-scale Ship. *Shipbuilding of China*, 63, 22-29. 1000-4882.

[29] Liang, L., Baoji, Z., Hao, Z., Jiaye, G., Zheng, T., Shuhui, G., Yuanbiao, B., Xu, Z. 2024. Study on numerical simulation and mitigation of parametric rolling in a container ship under head waves. *Brodogradnja*, 75(3), 75305. https://doi.org/10.21278/brod75305

[30] Umeda, N., Sakai, M., Fujita, N., Morimoto, A., Terada, D., Matsuda, A. 2016. Numerical prediction of parametric roll in oblique waves. *Ocean Engineering*, 120, 212-219. https://doi.org/10.1016/j.oceaneng.2016.05.014

[31] Sakai, M., Umeda, N., Yano, T., Maki, A., Yamashita, N., Matsuda, A., Terada, D. 2018. Averaging methods for estimating parametric roll in longitudinal and oblique waves. *Journal of Marine Science and Technology*, 23, 413-424. https://doi.org/10.1007/s00773-017-0490-6

[32] Gu, M., Bu, S.-X., Lu, J. 2020. Study of parametric roll in oblique waves using a three-dimensional hybrid panel method. *Journal of Hydrodynamics*, 32(1), 126-138. https://doi.org/10.1007/s42241-019-0029-x

[33] Pena, B., Muk-Pavic, E., Thomas, G., Fitzsimmons, P. 2020. An approach for the accurate investigation of full-scale ship boundary layers and wakes. *Ocean Engineering*, 214, 107854. https://doi.org/10.1016/j.oceaneng.2020.107854

[34] Sadat-Hosseini, H., Stern, F., Olivieri, A., Campana, E. F., Hashimoto, H., Umeda, N., Bulian, G., Francescutto, A. 2010. Head-wave parametric rolling of a surface combatant. *Ocean Engineering*, 37(10), 859-878. https://doi.org/10.1016/j.oceaneng.2010.02.010

[35] Zhang, H., Zhao, Z., Wei, Y., Liu, Y., Wu, W. 2025. A self-tuning variable universe fuzzy PID control framework with hybrid BAS-PSO-SA optimization for unmanned surface vehicles. *Journal of Marine Science and Engineering*, 13(3), 558. https://doi.org/10.3390/jmse13030558

[36] Xu, L., Huang, L., Zhao, X., Liu, J., Chen, J., Zhang, K., He, Y. 2025. Navigational decision-making method for wide inland waterways with traffic separation scheme navigation system. *Brodogradnja*, 76(2), 76201. https://doi.org/10.21278/brod76201

[37] Kriso. 2023. KCS Propeller Openwater Data (KRISO). *SIMMAN 2020 Workshop Benchmark Data*, Incheon, Korea. https://simman2020.kr/contents/KCS.php (accessed 30th July 2026)

[38] Shen, Z. 2014. Development of overset grid technique for hull-propeller-rudder interactions. *Doctoral Dissertation*, Shanghai Jiao Tong University, Shanghai, P.R.China.

[39] Kriso, Korea. 2015. Report of the Results for KCS Resistance & Self-Propulsion. *Tokyo 2015 Workshop on CFD in Ship Hydrodynamics*, Tokyo, Japan. https://t2015.nmri.go.jp./Instructions_KCS/instruction_KCS.html (accessed 30th July 2026)

[40] Han, S.-S., Dai, S., Terziev, M., Kim, D., Tezdogan, T., Jung, D., Song, S. 2025. Temperature-induced errors in ITTC model-ship extrapolation. *Journal of Marine Science and Engineering*, 13(7), 1203. https://doi.org/10.3390/jmse13071203

[41] Phuong, N. T. H., Taniguchi, T., Katayama, T. 2025. Numerical study of scale effects of viscous roll damping for a container ship. *Brodogradnja*, 76(4), 76406. https://doi.org/10.21278/brod76406